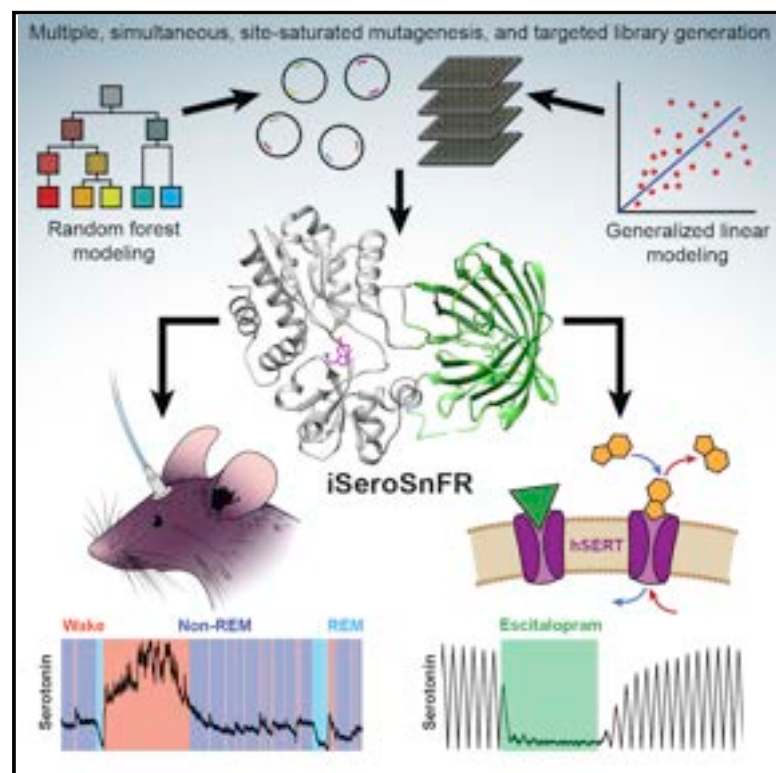


Directed Evolution of a Selective and Sensitive Serotonin Sensor via Machine Learning

Graphical Abstract



Authors

Elizabeth K. Unger, Jacob P. Keller, Michael Altermatt, ..., Viviana Gradinaru, Loren L. Looger, Lin Tian

Correspondence

loogerl@hhmi.org (L.L.L.),
lintian@ucdavis.edu (L.T.)

In Brief

Machine-learning-guided binding-pocket redesign enables engineering of genetically encoded sensor for serotonin that detects serotonin release in freely behaving mice and is used for the development of an assay for serotonin transporter function and modulation by drugs.

Highlights

- Developed a machine learning approach for rapid binding-pocket redesign
- Engineered a high dynamic range, sensitive, selective sensor for 5-HT: iSeroSnFR
- Demonstrated the use of iSeroSnFR for fiber photometry in awake behaving mice
- Developed a clinically relevant assay using iSeroSnFR for 5-HT transporter function



Resource

Directed Evolution of a Selective and Sensitive Serotonin Sensor via Machine Learning

Elizabeth K. Unger,^{1,12} Jacob P. Keller,^{2,9,12} Michael Altermatt,^{3,12} Ruqiang Liang,¹ Aya Matsui,⁵ Chunyang Dong,¹ Olivia J. Hon,⁶ Zi Yao,⁴ Junqing Sun,¹ Samba Banala,² Meghan E. Flanigan,⁶ David A. Jaffe,¹ Samantha Hartanto,¹ Jane Carlen,¹ Grace O. Mizuno,^{1,10} Phillip M. Borden,^{2,11} Amol V. Shivange,³ Lindsay P. Cameron,¹ Steffen Sinning,⁷ Suzanne M. Underhill,⁸ David E. Olson,¹ Susan G. Amara,⁸ Duncan Temple Lang,¹ Gary Rudnick,⁷ Jonathan S. Marvin,² Luke D. Lavis,² Henry A. Lester,³ Veronica A. Alvarez,⁵ Andrew J. Fisher,¹ Jennifer A. Prescher,⁴ Thomas L. Kash,⁶ Vladimir Yarov-Yarovoy,¹ Viviana Gradinaru,³ Loren L. Looger,^{2,*} and Lin Tian^{1,13,*}

¹Departments of Biochemistry and Molecular Medicine, Chemistry, Statistics, Molecular and Cellular Biology, and Physiology and Membrane Biology, the Center for Neuroscience, and Graduate Programs in Molecular, Cellular, and Integrative Physiology, Biochemistry, Molecular, Cellular and Developmental Biology and Neuroscience, University of California, Davis, Davis, CA 95616, USA

²Janelia Research Campus, Howard Hughes Medical Institute, Ashburn, VA 20174, USA

³Division of Biology and Biological Engineering, California Institute of Technology, Pasadena, CA 91125, USA

⁴Department of Chemistry, University of California, Irvine, Irvine, CA 92697, USA

⁵Laboratory on Neurobiology of Compulsive Behaviors, National Institute on Alcohol Abuse and Alcoholism, NIH, Bethesda, MD 20892, USA

⁶Bowles Center for Alcohol Studies, Department of Pharmacology, University of North Carolina School of Medicine, Chapel Hill, NC 27599, USA

⁷Department of Pharmacology, Yale University School of Medicine, New Haven, CT 06520, USA

⁸Laboratory of Molecular and Cellular Neurobiology, National Institute on Mental Health, NIH, Bethesda, MD 20892, USA

⁹Present address: Department of Pharmacology and Molecular Therapeutics, Uniformed Services University, Bethesda MD 20814, USA

¹⁰Present address: Seven Biosciences, 630 Pena Ave., Suite 400, Davis, CA 95618, USA

¹¹Present address: LifeEDIT, Research Triangle Park, NC 27709, USA

¹²These authors contributed equally

¹³Lead Contact

*Correspondence: loogerl@hhmi.org (L.L.), lintian@ucdavis.edu (L.T.)

<https://doi.org/10.1016/j.cell.2020.11.040>

SUMMARY

Serotonin plays a central role in cognition and is the target of most pharmaceuticals for psychiatric disorders. Existing drugs have limited efficacy; creation of improved versions will require better understanding of serotonergic circuitry, which has been hampered by our inability to monitor serotonin release and transport with high spatial and temporal resolution. We developed and applied a binding-pocket redesign strategy, guided by machine learning, to create a high-performance, soluble, fluorescent serotonin sensor (iSeroSnFR), enabling optical detection of millisecond-scale serotonin transients. We demonstrate that iSeroSnFR can be used to detect serotonin release in freely behaving mice during fear conditioning, social interaction, and sleep/wake transitions. We also developed a robust assay of serotonin transporter function and modulation by drugs. We expect that both machine-learning-guided binding-pocket redesign and iSeroSnFR will have broad utility for the development of other sensors and *in vitro* and *in vivo* serotonin detection, respectively.

INTRODUCTION

Serotonergic systems profoundly modulate diverse behaviors (Berger et al., 2009; Charnay and Léger, 2010). Serotonin (5-HT) dysregulation has been implicated in mental disorders, including depression and anxiety (Belmaker and Agam, 2008; Calhoun and Tye, 2015). Most antidepressants target some aspect of the serotonergic system; selective serotonin reuptake inhibitors (SSRIs) specifically target the 5-HT transporter (SERT) (Bos et al., 2012; Cipriani et al., 2018). Despite the critical importance of 5-HT, development of novel and more effective thera-

pies has been challenging due to poor understanding of 5-HT dynamics, specifically the inability to measure 5-HT with high spatiotemporal resolution. Existing methods for measuring 5-HT, including microdialysis and fast-scan cyclic voltammetry (FSCV) (Abdalla et al., 2017; Jaquins-Gerstl and Michael, 2015; Peñalva et al., 2003; Schultz and Kennedy, 2008), as well as transporter assays relying primarily on radiolabeled 5-HT or analogs (Clarke and Khalid, 2015), lack the spatial or temporal resolution to adequately probe 5-HT dynamics and targetability.

A genetically encoded 5-HT sensor could potentially overcome these technical challenges (for review, see Broussard

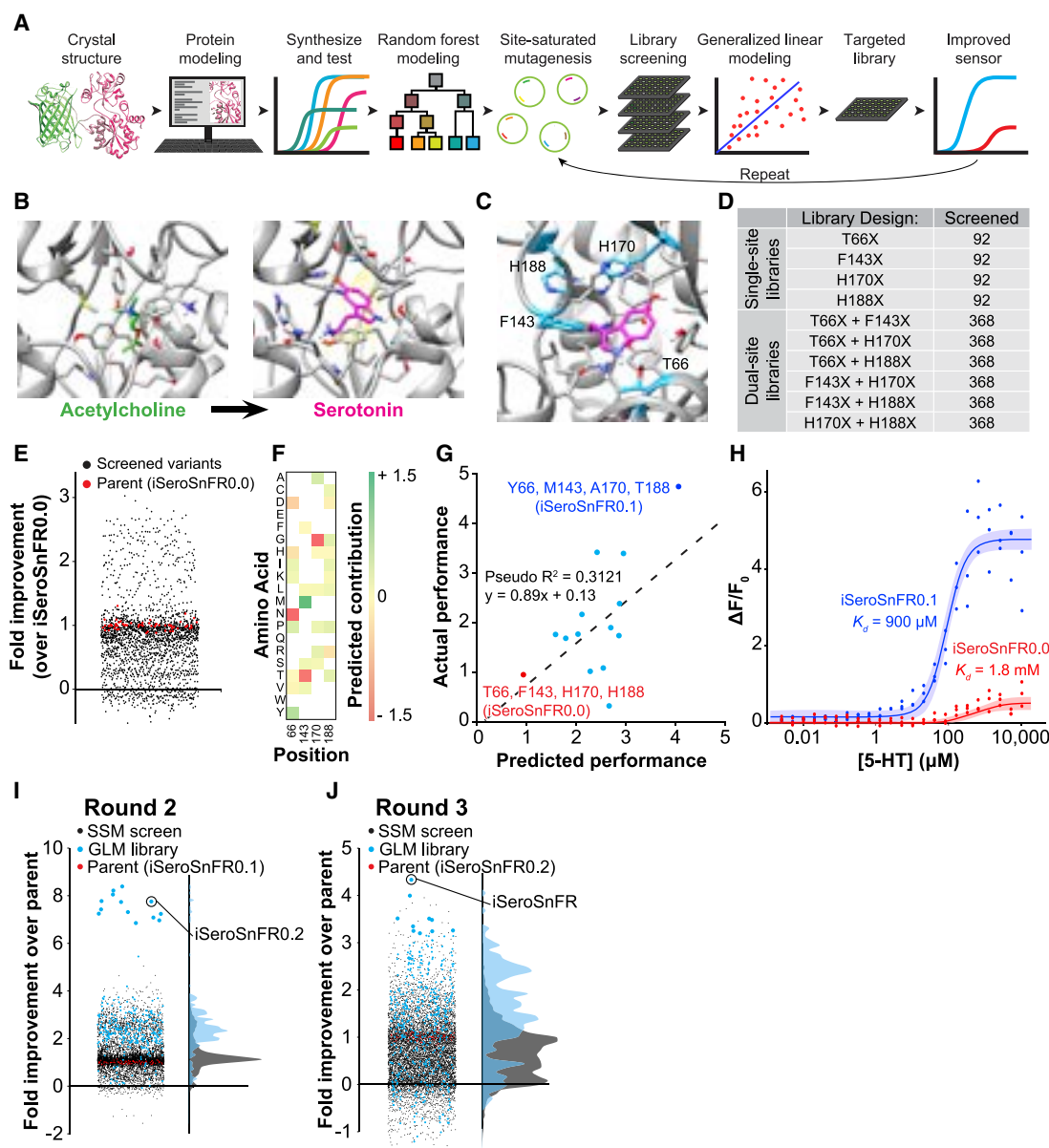


Figure 1. Using Machine Learning to Evolve Binding Proteins

(A) Overview of machine learning method.

(B) Schematic showing conversion of an acetylcholine (ACh)-binding protein to a serotonin (5-HT)-binding protein. ACh and 5-HT were docked into the binding pocket of AChSnFR0.6 using Rosetta. Statistical modeling was performed on these models, and promising mutations were synthesized and tested (see Figure S2 and Table S3). iSeroSnFR0.0 was chosen as a starting point for statistical modeling. Positions 66, 143, 170, and 188 were selected for further mutation.

(C) The binding pocket of iSeroSnFR0.0 was simulated using Rosetta and 5-HT (magenta) docked. Top-ranked positions are labeled (cyan).

(D) Table of DNA libraries created, and number of variants screened from each library.

(E) DNA libraries were generated, transformed into bacteria, grown, and lysed. Lysate was then screened with 10 mM 5-HT and compared to the parent sensor (iSeroSnFR0.0).

(F) Heatmap of the contribution of each mutation at each position screened, as predicted by the generalized linear model (GLM) (for additional information see Table S3).

(G) Combinations of mutations predicted to be better than the parent (iSeroSnFR0.0) were synthesized and tested as purified protein with 10 mM 5-HT. Dashed line represents the linear regression.

(H) Protein from iSeroSnFR0.0 and the top variant (iSeroSnFR0.1) was purified and tested against multiple concentrations of 5-HT. Fits were determined using the Hill equation. Shaded area denotes 95% confidence interval. The apparent K_d is defined as the concentration of the ligand producing 50% of the maximum fluorescence change.

(legend continued on next page)

et al., 2014; Lin and Schnitzer, 2016; Looger and Griesbeck, 2012). We and others have recently produced single-fluorescent protein (FP)-based sensors for neurotransmitters and neuromodulators based on either microbial periplasmic binding proteins (PBPs) or G-protein-coupled-receptors (GPCRs). Combined with modern microscopy, these sensors enable direct and specific measurements of diverse neurotransmitters and neuromodulators including glutamate (Marvin et al., 2013), GABA (Marvin et al., 2019), ATP (Lobas et al., 2019), dopamine (Patriarchi et al., 2018; Sun et al., 2018), acetylcholine (ACh) (Borden et al., 2020; Jing et al., 2020), and norepinephrine (Feng et al., 2019) with the necessary resolution for use in behaving animals (Corre et al., 2018; Madisen et al., 2015).

Although GPCR-based sensors can yield sensitive indicators, their response to pharmaceutical manipulations makes them problematic for use in any studies involving drug administration. Furthermore, it is difficult to target GPCR-based sensors to intracellular locations (e.g., to study 5-HT transport). PBP-based sensors are soluble and can therefore readily be targeted to subcellular locations, are amenable to high-throughput screening in bacteria, and easily allow detailed characterization in purified protein (Marvin et al., 2011). Naturally evolved PBPs typically bind few, if any, drugs targeting host proteins. In addition, microbial PBPs are bio-orthogonal to pathways in model organisms, promising minimal interference with endogenous signaling, a particular concern following long-term expression. Importantly, ligand binding in PBPs induces large conformational changes, resulting in very large dynamic ranges (Marvin et al., 2011, 2013, 2018). However, with no annotated PBPs for 5-HT, we opted to redesign the binding pocket of an existing PBP-based sensor to selectively bind 5-HT.

There are several complementary approaches available for binding-site redesign (Baker, 2019; Khoury et al., 2014). Site-saturated mutagenesis (SSM) combined with rational design can optimize sensor properties such as brightness, dynamic range, kinetics, and affinity (Cobb et al., 2013; Packer and Liu, 2015). However, SSM, while sufficient to convert our ACh sensor to one binding the cholinergic agonist nicotine (Shivange et al., 2019), cannot plausibly cover sufficient sequence space to radically change binding specificity to the structurally very different 5-HT. Computational design (Rosetta) can successfully predict proteins with high affinity and selectivity for a given small molecule (Richter et al., 2011), but has never been used for sensors. Recently, machine-learning approaches of varying complexity have been applied to optimize protein function (Bedbrook et al., 2019; Biswas et al., 2018; Ehren et al., 2008; Liao et al., 2007; Saito and Nakatsuji, 2001; Wu et al., 2019). Our approach combined computational design and machine learning to guide an SSM pipeline. Using this method, we developed the first PBP-based 5-HT sensor (iSeroSnFR) by redesigning the binding pocket of the ACh sensor iAChSnFR0.6 (Borden et al., 2020). iSeroSnFR contains 19 mutations relative to iAChSnFR0.6; these

conferred >5,000-fold improvement in 5-HT affinity while eliminating choline and ACh binding. We demonstrate that iSeroSnFR enables imaging of 5-HT dynamics in brain slices and freely moving mice. In addition, we highlight the clinical relevance of iSeroSnFR for pharmacological assays.

RESULTS

Sensor Design

Before redesigning a binding pocket for structurally disparate molecules, we established our machine learning pipeline on structurally similar molecules (Figure S1; Table S1; Data S1; STAR Methods). As a starting scaffold for our sensor, we chose an early version of iAChSnFR, based on a choline-binding PBP, OpuBC, from the hyperthermophile *Thermoanaerobacter* sp. X513 (Miller et al., 2011). In addition, this variant displayed detectable binding to 5-HT (apparent $K_d > 1$ mM) (Figure S2A), making it a good starting template. We used a multi-stage pipeline to iteratively improve 5-HT binding and sensor response (Figure 1A). We first performed computational binding-pocket redesign using Rosetta, then iterative rounds of SSM guided by machine learning.

Step I: Computational Binding-Pocket Redesign

To perform computational modeling, we started with the structures of open, ligand-free iAChSnFR0.6 (6URU) and closed, choline-bound *Bacillus subtilis* OpuBC (3R6U), and created a model of the closed, ACh-bound form of iAChSnFR using Rosetta (Figure 1B). 5-HT conformers (rotation of the β -aminoethyl and hydroxy moieties) were generated using Open Eye Omega (Hawkins et al., 2010), and docked into the closed-iAChSnFR model using RosettaLigand (Bender et al., 2016; Davis and Baker, 2009) (Figures 1B and 1C). Next, Rosetta protein redesign (Taylor et al., 2016; Tinberg et al., 2013) was used to optimize the 5-HT binding pocket. In total, 250,000 variants were predicted and ranked based on computed ligand interaction (STAR Methods). The top 18 predicted variants were synthesized, purified, and examined for fluorescence response to 5-HT and other ligands including ACh (Figures S2B and S2C). Among the 18 variants, variant 7 showed the largest fluorescence response to 10 mM 5-HT ($\Delta F/F_0 = 87\% \pm 20\%$) with no ACh response ($\Delta F/F_0 = -4\% \pm 1\%$), representing an 18-fold improvement in 5-HT selectivity (Figure S2C). This mutated variant, named iSeroSnFR0.0 (Table S2), was then selected for further optimization.

Step II: Random Forest Modeling

We next optimized iSeroSnFR0.0 with SSM to improve 5-HT affinity. We used a random forest (RF) model to estimate the importance of each position interrogated by computational design (Table S2). We took the four highest-ranked positions from RF (66 > 170 > 143 > 188) (Figure 1D) and performed SSM at each site separately and in pairs (using degenerate NNK codons). We

(I) Raincloud plot where iSeroSnFR0.1 was used as the parent for a second round of screening followed by GLM analysis. A small library (32 possible combinations) was generated based on the GLM results and screened (cyan), which led to the discovery of iSeroSnFR0.2.

(J) Raincloud plot similar to (I), but using iSeroSnFR0.2 as the parent. This GLM-guided targeted library (96 possible combinations) was created and screened, leading to the discovery of iSeroSnFR.

See also Figures S1 and S2 and Data S1.

screened a total of 2,576 variants, including 92 from each single-site library and 368 from each dual-site library, for fluorescence response to 5-HT (10 mM). The library size was determined using the TopLib online library calculator (Nov, 2012). Of the screened variants, ~100 variants showed an improved response (~2- to 3-fold) compared to iSeroSnFR0.0 (Figure 1E). Subsequent analysis showed that top-performing variants frequently contained mutations at multiple positions, and the ordered contribution of each position (66 > 143 > 170 > 188) (Table S2) to the fluorescence response was nearly identical to that predicted by RF (66 > 170 > 143 > 188) (Figure 1F). No single mutation drastically improved 5-HT affinity, but combinations of mutations were frequently better than single mutations (Figure S2D). These results suggest that RF effectively predicts important positions contributing to sensor response, and simultaneous, beneficial contributions of multiple residues are essential to large-scale improvements.

Step III: Generalized Linear Model

Because single mutations offered only small improvements, whereas combinations gave much better results, mutations were clearly not additive. For example, we found a top-performing variant containing T66Y/H170A with 140% improved response, whereas T66Y and H170A alone showed only 40% and 10% improvements, respectively (Figure S2D). We next applied GLM to our dataset. This allowed us to identify individual mutations from our libraries that contribute to synergistic interactions—allowing us to design small targeted libraries.

GLM predicted that several amino acid mutations at each position would be beneficial (Figure 1F; Table S3), with 66Y, 66P, 143M, 170A, 188G, 188P, and 188T showing the strongest positive predictions. Given the beneficial T66Y/H170A mutant that we had already identified, we decided to synthesize variants combining those with GLM-predicted amino acid residues at positions 143 and 188. Out of 13 variants synthesized, 12 showed larger fluorescence response to 10 mM 5-HT than iSeroSnFR0.0 (Figure 1G) (GLM was moderately predictive: pseudo- $R^2 = 0.31$). One variant displayed 4.5-fold improved response over iSeroSnFR0.0, well above any SSM-screened variant. In purified protein, this variant (T66Y/F143M/H170A/H188T, named iSeroSnFR0.1) showed >9-fold increased fluorescence response ($(\Delta F/F_0)_{\max}$ relative to iSeroSnFR0.0 $(\Delta F/F_0)_{\max} = 480\% \pm 14\%$ versus $50\% \pm 4\%$), and 2-fold increased 5-HT affinity ($900 \pm 110 \mu\text{M}$ versus $1.8 \pm 0.5 \text{ mM}$) (Figure 1H).

In light of the substantial improvements from a single round of GLM-guided mutagenesis, we performed two more rounds of screening followed by GLM prediction, recruiting additional positions predicted by RF, and added others based on prior experience optimizing biosensors (e.g., linkers connecting the cpGFP to the binding protein, the interface between cpGFP and binding protein, and random mutations from previous rounds of screening) (Table S2). These subsequent rounds were screened at progressively lower 5-HT concentrations (round 2: 500 μM and round 3: 50 μM) to enrich for variants with tighter affinity. After each round, the top-performing variants were sequenced and re-analyzed using GLM to create a focused library; in total, ~13,000 variants were tested, of which 244 were sequenced. The best variant from round 2 (Figure 1I) came from the GLM-driven

focused library, had 8-fold improved response over its parent iSeroSnFR0.1, and was named iSeroSnFR0.2. The best variant from round 3 (Figure 1J) was 5-fold improved over its parent iSeroSnFR0.2 (Figure 2A; Table S2). We named this final version iSeroSnFR, which contains 19 mutations relative to iAChSnFR0.6 (Figure 2A, PDB: 6PER); In purified protein, this variant exhibits $310 \pm 30 \mu\text{M}$ affinity for 5-HT, and 800% ($\Delta F/F_0)_{\max}$ (Figure 2B).

Our data show that GLM is highly effective at identifying beneficial mutations (Figures 1I and 1J): the average performance of GLM variants was significantly higher than SSM variants (1st, 2nd, and 3rd rounds: $p < 0.001$, Wilcoxon rank-sum test) and more importantly, the top variants in each round (including the top 15 variants from round 2) were from the GLM-inspired library as opposed to the SSM library. Thus, our machine-learning-guided mutagenesis pipeline can improve protein-ligand binding selectivity and affinity even for target molecules structurally distant from cognate ones, while still maintaining sensor function.

In Vitro Characterization

iSeroSnFR is highly specific for 5-HT over a wide array of endogenous molecules and drugs (Figures 2C and S3). Only tryptamine and dopamine showed detectable responses, but with 8- and 16-times weaker affinity (apparent $K_d = 2.4 \text{ mM}$ for tryptamine and 5.6 mM for dopamine), respectively. Other endogenous molecules showed marginal responses, with very low or negative responses, and/or titrations that did not fit a single-site binding isotherm.

To determine the *in situ* affinity in mammalian (HEK293T) cells, we cloned iSeroSnFR into the pMinDisplay expression vector (pDisplay lacking the HA epitope tag) (Marvin et al., 2013) such that iSeroSnFR would be displayed on the outer cell surface; we also cloned a version targeted to the post-synapse using full-length neuroligin (Nlgn) (STAR Methods). We observed robust membrane localization (Figure 2D) and clear response to 1.6 μM 5-HT (~50% $\Delta F/F_0$) (Figures 2E and S4A). The *in situ* affinity of the sensor on HEK293T cells was similar ($390 \pm 110 \mu\text{M}$) to that in purified protein. Fortuitously, the fluorescence response of iSeroSnFR on HEK293T cells was significantly increased ($(\Delta F/F_0)_{\max} = 1,700\%$). To characterize the utility of iSeroSnFR for physiologically relevant concentrations, we focused on the range from high-pM (338 pM) to mid- μM (60 μM) (Figures 2F and S4B). We observed small but reliable responses to all concentrations tested ($\Delta F/F_0 = 16.8\% \pm 1.9\%$ at 338 pM; similar responses up to 246 nM 5-HT) (Figure S4B). We quantified the ability of iSeroSnFR to faithfully report 5-HT by comparing 5-HT responses to Hank's balanced salt solution (HBSS) buffer responses (Figure S4C) with two metrics from signal detection theory: the receiver operating characteristic (ROC) (Figure S4D) and the discriminability index (d') (Figure S4E). ROC analysis indicates that 5-HT responses show essentially perfect discrimination (area under the curve = 0.990) (Figure S4D, bottom) of true-positives from false-positives, whereas buffer responses have no power (Figure S4D, top). Similarly, d' analysis shows that 5-HT responses have very strong separation from system noise ($d' > 3$) (Figure S4E, bottom), but buffer responses show essentially no separation (Figure S4E, top). Results on the surface of dissociated

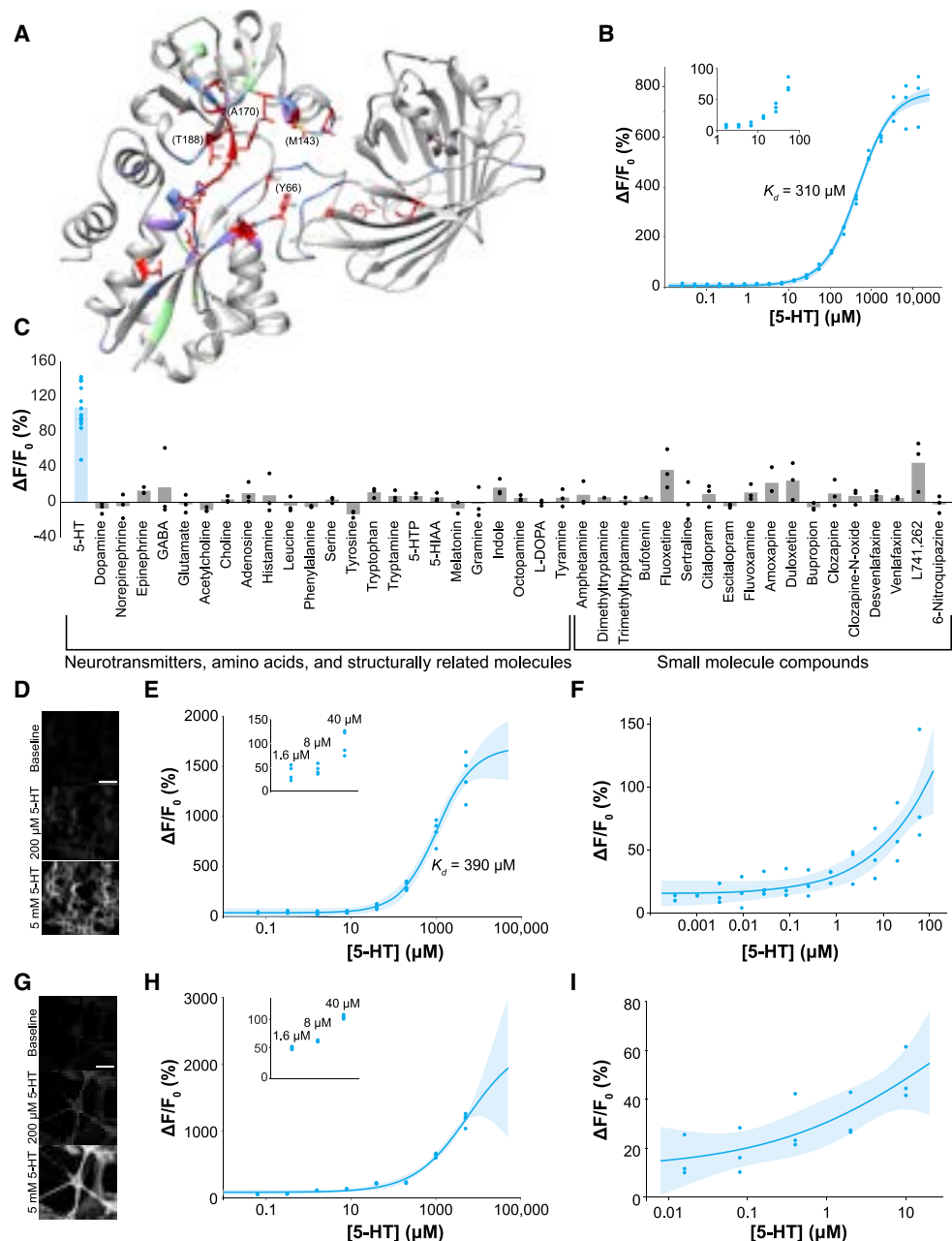


Figure 2. Affinity and Specificity of the Sensor

(A) Crystal structure of unliganded iSeroSnFR (PDB: 6PER). Mutations in iSeroSnFR relative to iAChSnFR0.6 are mapped onto the crystal structure (red). Positions interrogated by site-saturated mutagenesis (but not mutated in iSeroSnFR) are displayed in blue, mutations interrogated by Rosetta, but not SSM, in purple, and positions that were randomly mutated, in green.

(B) Purified iSeroSnFR binding to 5-HT.

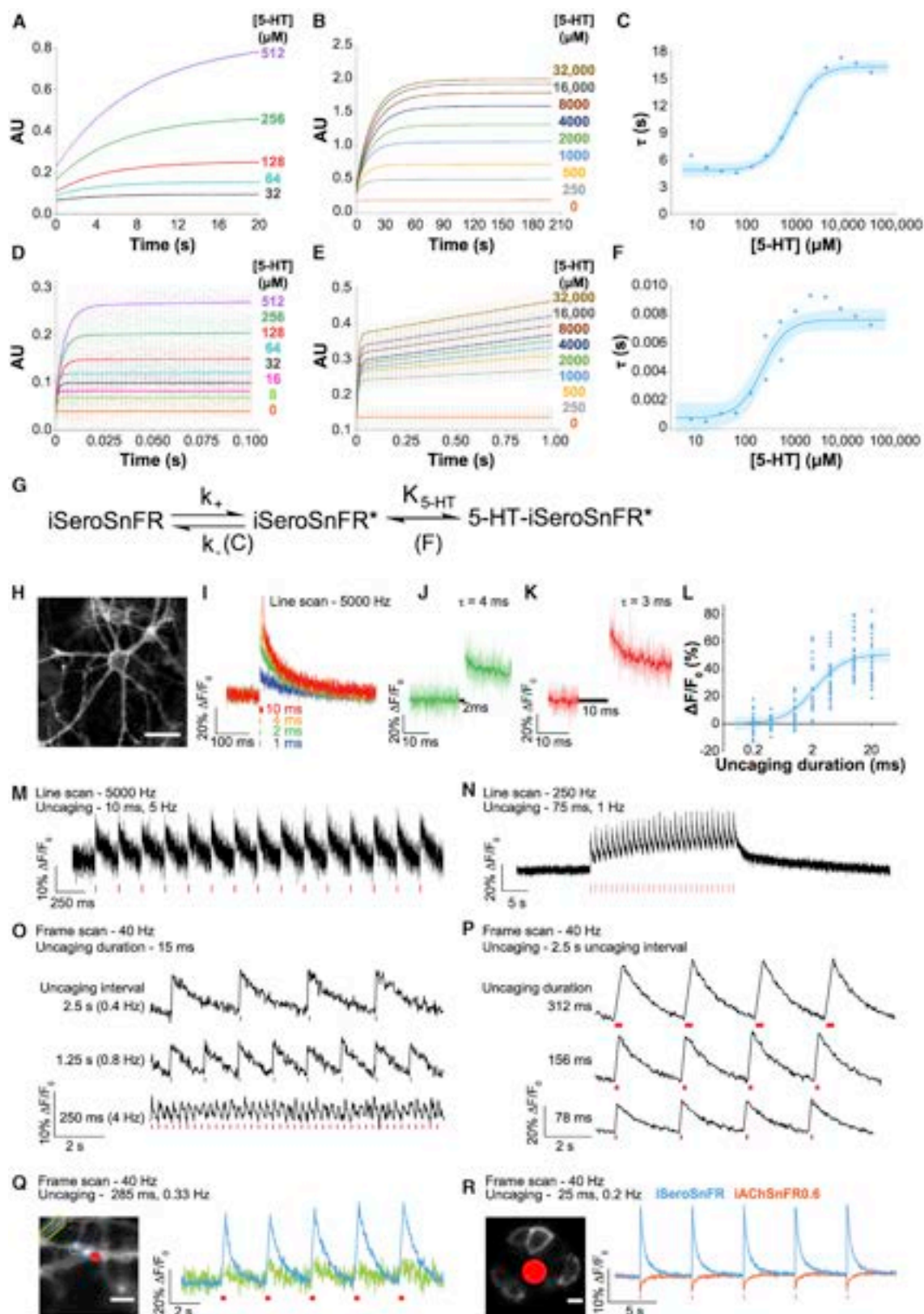
(C) Purified iSeroSnFR binding to multiple ligands. Due to differential compound solubility, the values displayed match the following concentrations: octopamine, L-phenylalanine, 80 μM ; 5-HTP, 85 μM ; sertraline, 110 μM ; L-DOPA, tyramine, escitalopram, citalopram, amoxapine, 125 μM ; all other compounds were tested at either 100 or 105 μM . For the full concentration curve for each compound, see [Figure S3](#).

(D–F) Response of membrane-displayed iSeroSnFR in HEK293T cells. Representative images (D), and dose-response curves for higher concentrations (E) and lower concentrations (F). $n = 3–4$.

(G–I) Response of membrane-displayed iSeroSnFR-PDGFR in cultured neurons. (G–I) Representative images (G), and dose-response curve for higher concentrations (H) and lower concentrations (I). $n = 3–4$. For raw traces, see [Figure S4](#).

(B, E, F, H, and I) Fits were determined using the Hill equation. Shaded area denotes 95% confidence interval. Scale bars represent 50 μm . Insets show magnifications of the points at low concentrations.

See also [Figures S3 and S4](#).



(legend on next page)

hippocampal neurons were similar to those on HEK293 cells ($\Delta F/F_0 = 15.8\% \pm 2.0\%$ at 16 nM 5-HT) (Figures 2G–2I and S4F).

We next sought to assess sensor kinetics. Using stopped-flow fluorescence, we found that the sensor reached saturation after ~10–40 s (Figures 3A and 3B). With a single exponential fit, τ_{apparent} was between 5 and 18 s (Figure 3C). We noted, however, that there appeared to be a very fast and robust initial rise (Figures 3D and 3E). We therefore fit a double-exponential curve with two phases of activation: a fast initial rise (Figure 3F), and a slower rise to saturation. Our double-exponential fit the data much more precisely and showed that the two phases occur with a rise τ of 0.5–10 ms (fast) and 5–18 s (slow). We postulate that ligand binding rapidly activates fluorescence of the sensor (Figure 3G, $K_{5\text{-HT}}$), but that the sensor in purified protein exists in an “inactive” (iSeroSnFR) and an “active” (iSeroSnFR*) conformation, and the transition between these states is slow (Figure 3G, k_+).

We then validated the kinetics of iSeroSnFR by using light-evoked release of 5-HT from a caged version (PA-N-5HT). Single pulses (1 ms) of uncaged 5-HT were robustly detected on the surface of cultured neurons (Figures 3H and 3I), and the amplitude of fluorescence changes increased with uncaging pulse duration (Figures 3J–3L). Decay to baseline featured a fast component ($\tau_{\text{decay}} \sim 4$ ms at 10 ms pulse duration) followed by a slower component ($\tau_{\text{decay}} \sim 150$ ms at 10 ms pulse duration) (Figures 3J and 3K). Diffusion of uncaged 5-HT away from the imaging location likely explains the slower component. To determine how iSeroSnFR responds to repeated 5-HT bursts, we used various combinations of uncaging pulse durations and frequencies. One-photon line-scans at 5,000 Hz or 250 Hz, and frame-scans at 40 Hz revealed robust, reproducible fluorescence increases to trains of uncaging pulses at various frequencies over prolonged imaging (line scans: 10 ms uncaging pulses at 5 Hz, Figure 3M, and 75 ms uncaging pulses at 1 Hz, Figure 3N; frame scan: 15 ms uncaging pulses at 0.4, 0.8, and 4 Hz, Figure 3O). Fluorescence response amplitude increased with uncaging pulse duration under frame-scan (Figure 3P). However, when line-scan mode was used, the amplitude decreased with increased pulse frequency (Figures 3O and S5A), possibly due to accumulation of 5-HT in the bath and resulting sensor saturation. It is also possible that this results

from the slow phase of the sensor response, as described above. 5-HT uncaged at one dendrite produced a negligible response in dendrites ~10 μm away (Figure 3Q). Although 5-HT uncaging readily activated iSeroSnFR, it failed to activate iAChSnFR0.6 (Figure 3R), indicating that the fluorescence response is specific to release of 5-HT, and not artefactual.

Imaging Endogenous Release of 5-HT in Brain Slice

Serotonergic fibers from the raphe nuclei innervate many brain regions, with dense projections found in medial prefrontal cortex (mPFC), orbitofrontal cortex (OFC), striatum, bed nucleus of the stria terminalis (BNST), and basolateral amygdala (BLA) (Bang et al., 2012; Belmer et al., 2017; Zhou et al., 2015). To demonstrate iSeroSnFR's utility in mouse brain slices, we first examined the expression level of iSeroSnFR in striatum and in mPFC. We cloned iSeroSnFR into regular and Cre-dependent adeno-associated virus (AAV) backbones, producing AAV2/9.CAG.iSeroSnFR.Nlgn and AAV2/9.CAG.FLEX.iSeroSnFR.PDGFR. We injected AAV2/9.CAG.iSeroSnFR.Nlgn into dorsal striatum of C57BL/6J mice (Figure 4A), and a mix of AAV2/9.CAG.FLEX.iSeroSnFR.PDGFR and AAV2/9.CMV.Cre (9:1 ratio) into mPFC of *Rosa^{l14/+}* (Cre-dependent tdTomato expression) (Madisen et al., 2010) (Figure S5B). After 2 weeks recovery, iSeroSnFR expression was obvious in dorsal striatum as evidenced by widespread green fluorescence (Figure 4B) and in mPFC as evidenced by green fluorescence on membranes and processes of red, Cre-positive neurons (Figure S5C). We demonstrated robust functionality by imaging iSeroSnFR with two-photon frame-scan imaging while applying exogenous 5-HT via microinjection (Figures S5D–S5F), or by imaging iSeroSnFR with one-photon photometry and applying exogenous 5-HT via bath application (Figure S5G).

We next imaged iSeroSnFR responses to electrically triggered release in mouse brain slices using one-photon photometry. Brief electrical stimuli triggered 5-HT release, readily detected by iSeroSnFR (1 pulse: $\Delta F/F_0 = 0.71\% \pm 0.12\%$); response amplitudes correlated with the number of electrical stimuli ($\Delta F/F_0 = 1.1\% \pm 0.1\%$ [2 pulses], $2.0\% \pm 0.4\%$ [5 pulses], $2.8\% \pm 0.5\%$ [10 pulses], $4.1\% \pm 0.7\%$ [20 pulses], and $5.8\% \pm 0.9\%$ [40 pulses], $n = 7$) (Figures 4C and 4D). Surprisingly, neither amplitude nor decay kinetics of fluorescence transients was affected by bath application of cocaine (10 μM), citalopram (1 μM), or

Figure 3. Sensor Kinetics

(A–F) iSeroSnFR was purified and tested in a stopped-flow apparatus, with increasing concentrations of 5-HT.

(A and B) Average traces showing full time courses for low (A) and high (B) concentrations.

(D and E) Magnification of the first 100 ms and 1 s, respectively, of the data in (A) and (B), respectively, with double exponential fits shown.

(C and F) The τ (1/rate constant) for each concentration for the slow phase (C) and the fast phase (F) was fit using the Hill equation. Shaded area denotes 95% confidence interval.

(G) Model of iSeroSnFR function showing two rate-limiting steps: isomerization between the inactive and active states, followed by binding of serotonin, for full fluorescence activation. $n = 16$ –18 trials for each concentration.

(H–R) Primary cultured neurons (H–Q) and HEK cells (R) were exposed to 200 μM caged-5-HT (PA-N-5-HT) and uncaged using 405 nm laser stimulation.

(H) Representative image.

(I) 5-HT was uncaged as noted. Traces represent a 9-trial average for each replicate. Biological replicates = 3. There was no image acquisition during 405 nm laser stimulation.

(J and K) Data expanded from (I). Faded lines depict raw traces, dark lines represent average traces.

(L) Data from (I) was plotted and fit with using the Hill equation. Shaded area denotes 95% confidence interval.

(M–R) 5-HT was uncaged as noted. Red lines represent uncaging epochs.

(M and N) Line scans (128 \times 1 pixel) at 5 kHz (M) and 250 Hz (N).

(O–R) Frame scans (128 \times 128 pixel) at 40 Hz. For raw traces, see Figure S5. (Q) Red dot represents uncaging spot. Blue and green traces represent data from regions of interest outlined on the image (~2 μm and ~20 μm from the uncaged region). (R) Response of membrane-displayed iSeroSnFR and iAChSnFR0.6 to serotonin uncaging on HEK293T cells. Scale bars represent 50 μm (H) and 10 μm (Q and R).

See also Figure S5.

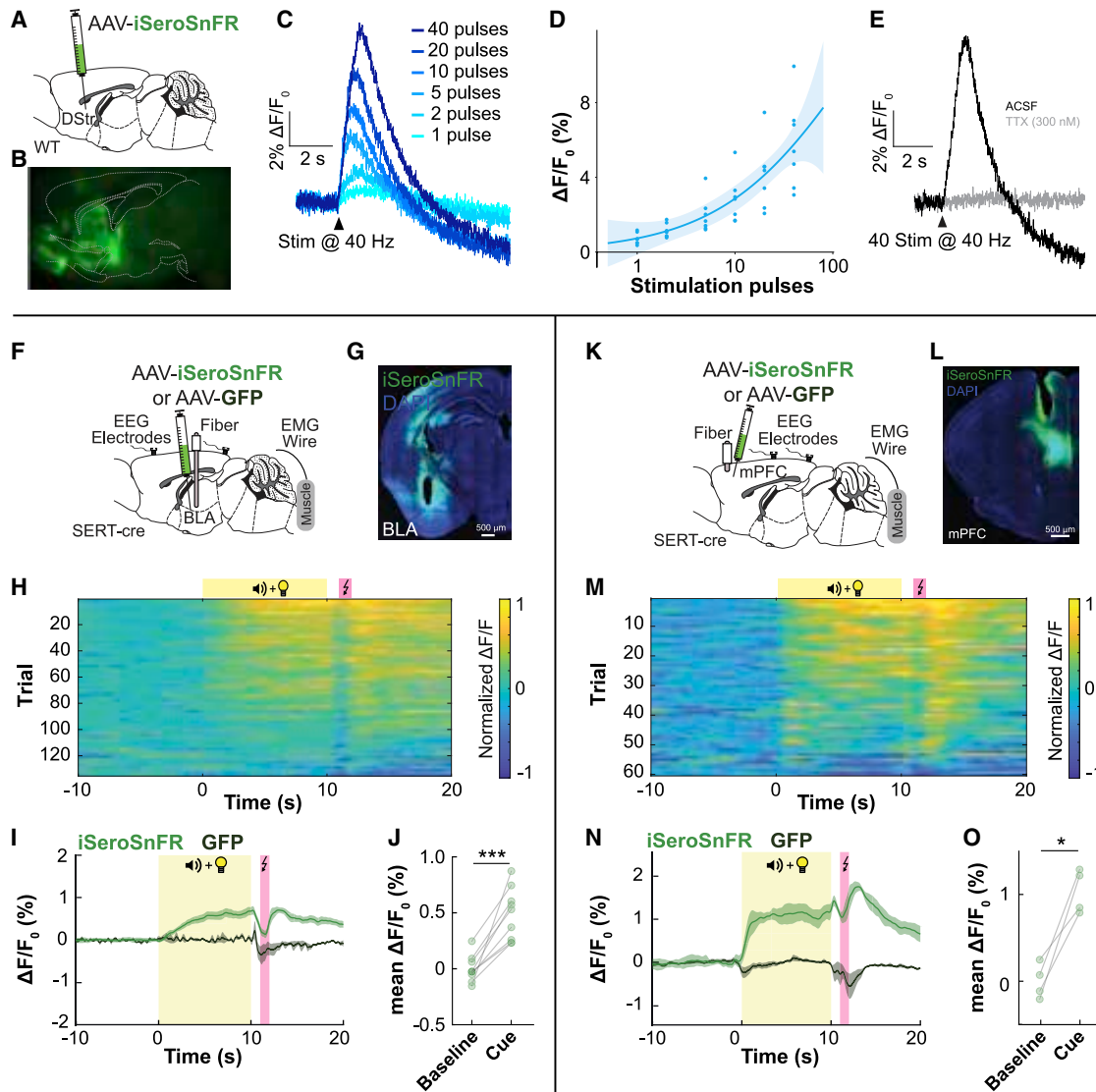


Figure 4. Detection of Electrically or Behaviorally Triggered Release of 5-HT

(A–D) WT mice were injected with AAV2/9.CAG.iSeroSnFR.Nlgn into the dorsal striatum (DStr). Slices were prepared (300 μ m) and imaged using one-photon photometry.

(A and B) Schematic (A) and representative (B) image of sensor injection and expression.

(C) Slices were stimulated using a monopolar saline-filled glass electrode (0.5 ms; 50 μ A) at the frequencies noted.

(D) Data from (C) fitted using the Hill equation. Shaded area represents 95% confidence interval.

(E) Tetrodotoxin (TTX; 300 nM) was added to the perfusion solution, and the slice was stimulated at 40 Hz for 1 s ($n = 11$ slices from 3 mice). For more information, see Figure S5.

(F–O) Fiber-photometry recording of 5-HT release in response to fear-conditioning in BLA (F–J) and mPFC (K–O). Mice were injected with either AAV2/9.CAG-iSeroSnFR.Nlgn or AAV2/5.CAG-GFP (as a negative control) followed by optical fiber implantation into BLA (F and G) or mPFC (K and L). Yellow box indicates unconditioned stimulus (tone + house lights); pink box illustrates foot shock. Single-trial traces (H and M) or average trace across all trials (I and N). Shaded area represents SEM. Statistical comparison was made based on the average fluorescence for the 10 s before the cue onset (baseline) and the 10 s of cue presentation (J and O). $N = 15$ trials/animal, $n = 9$ BLA^{iSeroSnFR}, 3 BLA^{GFP}, 4 mPFC^{iSeroSnFR}, and 3 mPFC^{GFP}. * $p < 0.05$, *** $p < 0.001$, paired Student's *t* test.

See also Figure S5 and S6.

reserpine (1 μ M) (Figure S5H). Importantly, however, tetrodotoxin (TTX, 300 nM) (Figure 4E) completely abolished electrically evoked fluorescence transients, indicating that signals are indeed action potential-dependent.

Imaging Endogenous Release of 5-HT in Freely Behaving Mice

We then examined the utility of iSeroSnFR in reporting physiologically relevant 5-HT dynamics in freely behaving mice across

multiple brain regions (Figure 4F–O). Serotonergic DRN neurons respond to both rewarding and aversive stimuli, but little is known about the dynamics of 5-HT release in regions receiving inputs from DRN (Li et al., 2016; Ren et al., 2018). Multiple lines of evidence highlight 5-HT as a critical neuromodulator of fear learning (Bocchio et al., 2016; Burghardt et al., 2007; Marcinkiewicz et al., 2016). Therefore we injected AAV2/9.CAG.iSeroSnFR.Nlgn or AAV2/9.CAG.GFP into BLA (Figures 4F and 4G) and mPFC (Figures 4K and 4L), followed by fiber photometry during a fear learning paradigm. Mice were trained for 15 trials (Curzon et al., 2009), during which a cue period (10 s tone and light) was followed by a 1-s pause, and then a 1-s footshock (Figures 4H–4J and 4M–4O). We observed a rise in 5-HT during the cue period that was immediate in mPFC but slower in BLA, followed by a dip during the footshock and further rise afterward that decayed slowly in both brain regions, which was reliable across individual trials (Figures 4H and 4M). In control GFP-expressing mice, smaller deflections were associated with cue onset and foot shock, likely due to motion artifacts (Figures 4I and 4N).

We next imaged 5-HT release in response to social interaction in multisite recordings in three brain regions simultaneously: OFC, BNST, and BLA, which are suggested to mediate this behavior in different ways (Kiser et al., 2012). We injected AAV2/9.CAG.iSeroSnFR.Nlgn into all three regions (Figures S6A–S6D) followed by multi-site fiber photometry during introduction of a same-sex intruder (Figure S6E). Wheel running has been shown to buffer behavioral consequences of stress in rodents, with concomitant changes in presynaptic 5-HT receptor and transporter expression in DRN (Greenwood et al., 2005). To assess this, we allowed mice access to a functional running wheel for 6 weeks prior to social interaction testing (Figure S6E). We found that iSeroSnFR reliably detected changes in 5-HT release during intruder presentation (Figures S6F–S6K; both in red “run” and blue “locked” trials), consistent with reports that DRN^{5-HT} cells are activated by social interaction (Li et al., 2016). This increase was similar across all three regions, reaching statistical significance in OFC and BLA (Figures S6I–S6K). Free access to the wheel significantly increased 5-HT signal peak during social interaction, but only in OFC (Figures S6F–S6K; red “run” versus blue “locked”). Taken together, these data suggest that iSeroSnFR permits robust recording of 5-HT release triggered by fear conditioning and social interaction and behavioral modulation by wheel-running in multiple brain regions.

Imaging 5-HT Dynamics in Sleep-Wakefulness Cycles

We next tested the utility of iSeroSnFR in reporting 5-HT dynamics over long time intervals in sleep-wakefulness cycles (Portas et al., 2000). Electroencephalographic (EEG) and electromyographic (EMG) electrodes were implanted for simultaneous polysomnographic (sleep) recordings (Figures 5A and S7A). iSeroSnFR tracked 5-HT fluctuations across sleep-wake cycles over prolonged times, correlating well with EEG/EMG signals (Figures 5B and S7B). When variable durations of sleep-wake states were normalized, iSeroSnFR signal amplitude was highest in wakefulness, decreased during non-rapid eye movement (NREM, “slow-wave”) and was lowest during rapid eye movement (REM, “paradoxical”) sleep (Figures 5C and S7C). We then examined 5-HT

dynamics during state transitions. Fluorescence signals rose sharply at waking, peaked during wakefulness, and decreased immediately after sleep onset, further decreasing during REM sleep. The largest signal increase occurred during the REM-to-wakefulness transition, and the largest decrease was from non-rapid eye movement (NREM)-to-REM (Figures 5D and S7D), clearly visible in individual trials. In control mice expressing GFP, no behavioral state-dependent changes in fluorescence were observed. Similar patterns were observed in both mPFC and BLA, however, in BLA, we observed more prominent fluorescence decreases during wakefulness-to-NREM transitions.

SERT Function and Pharmacology in Cell Culture

Given the clinical significance of drugs affecting 5-HT signaling and transport, we developed an iSeroSnFR-based assay to functionally characterize hSERT and drugs modulating it. We previously developed the oscillating stimulus transporter assay (OSTA) using intracellularly expressed fluorescent sensors for glutamate (Keller and Looger, 2016) and glucose (Keller et al., 2019). Because iSeroSnFR is intracellularly targetable, and does not respond to most clinical drugs, it is ideal for use with OSTA to assess hSERT-mediated transport (Figure 6A).

We first confirmed reported ionic requirements for hSERT function (reviewed in Rudnick and Sandtner, 2019). Extracellular sodium (10 or 160 mM) and chloride (10 or 160 mM) were both required for 5-HT uptake, while high extracellular potassium (150 mM) in the absence of sodium and 5-HT drove efflux, without dependence on chloride (Figures 6B and 6C). We next measured hSERT's K_m for sodium in 5-HT uptake by subjecting cells to a smoothly varying ramp of external sodium concentration, interleaved with high sodium (150 mM) bouts, verified using the dye sulforhodamine 101 (200 mM). (Figure 6D). Uptake rates in individual cells were plotted as a function of $[Na^+]$ and fitted using the Hill equation, yielding an average K_m of 6.5 ± 0.1 mM and a Hill coefficient of 1.9 ± 0.1 (Figures 6E and 6F), similar to published values (Koldso et al., 2011; Sneddon, 1969). These results demonstrate that intracellularly expressed iSeroSnFR can precisely quantify transporter biophysical properties.

We next used this technique to investigate drugs targeting hSERT. Drugs were added to both influx and efflux buffers to ensure consistent exposure. As expected, 5-HT transport was reduced by the competitive inhibitor cocaine (10 μ M) (Figure 6G). Similarly, the SSRI escitalopram rapidly diminished 5-HT transport by >50% at 500 nM and abolished it at 1 μ M (Figures 6H and 6I). The tricyclic antidepressant clomipramine (100 nM) also inhibited 5-HT transport, but with slower on- and off-rates than escitalopram (Wang et al., 2013) (Figure 6J). A newer antidepressant, vilazodone, caused transport function to rapidly disappear, and despite washouts of >20 minutes, did not return to baseline (Figure 6K). Because vilazodone's reported K_i (0.5 nM) (Heinrich et al., 2004) is comparable to that of clomipramine (0.3 nM) (Tatsumi et al., 1997), this result was unexpected and requires further investigation. We next measured longitudinal effects of stimulation of the protein kinase C pathway through addition of phorbol 12-myristate 13-acetate (PMA), which decreases 5-HT transport (400 nM) (Bermingham and Blakely, 2016). PMA induced a slow decrement in transport rate over ~40 minutes, consistent with its reported effects (Figure 6L)

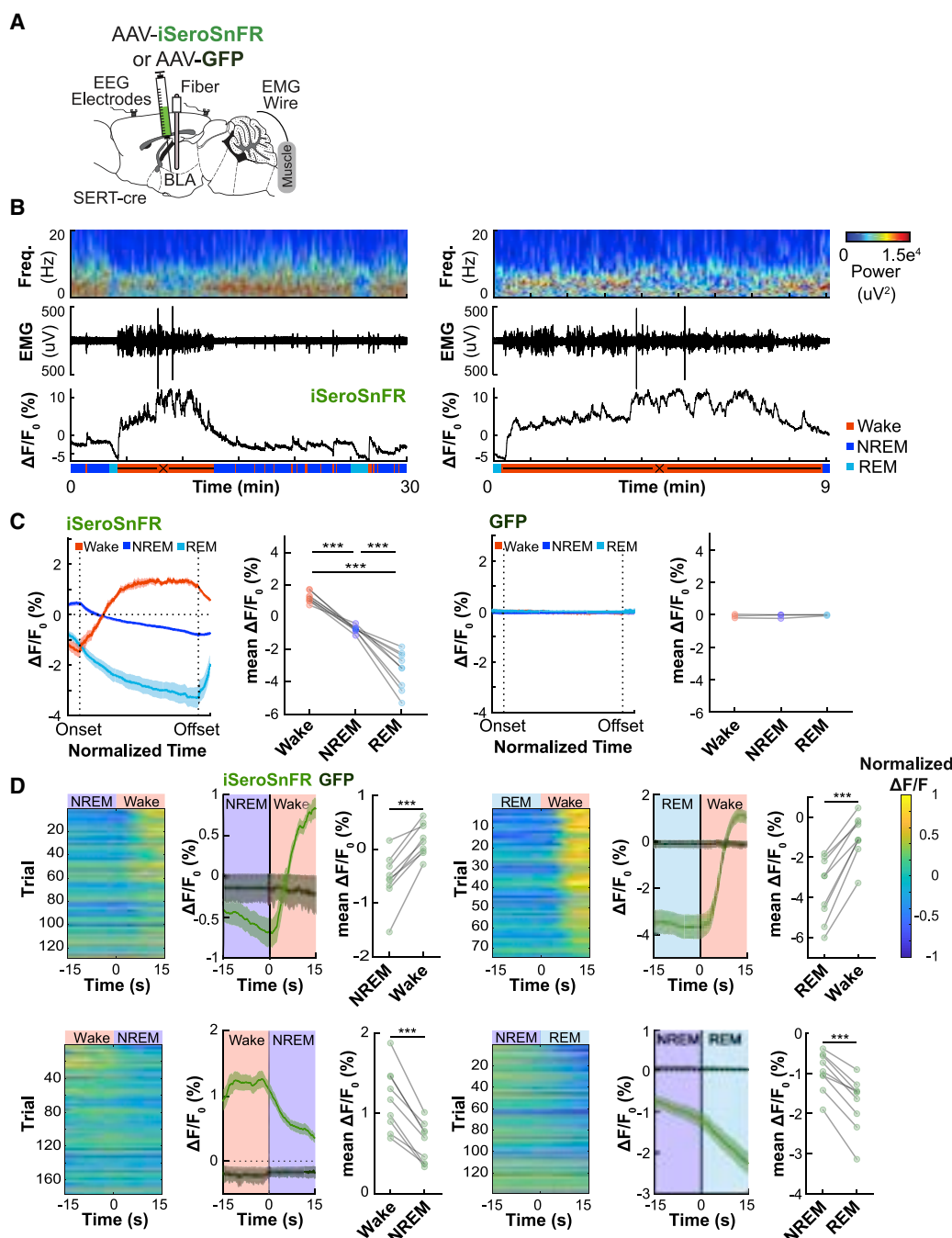


Figure 5. Detection of 5-HT Release during Sleep-Wakefulness Cycles in BLA

(A) Mice were injected with either AAV2/9.CAG-iSeroSnFR.Nlgn or AAV2/5.CAG-GFP (as a negative control), and an optical fiber was implanted into basolateral amygdala (BLA). EEG screw electrodes and EMG wires were implanted to classify sleep-wake states.

(B) Representative BLA^{iSeroSnFR} EEG spectrograms, EMG, and fiber photometry traces over time across sleep-wake cycles (left) and walking episode (right).

(C) Temporal dynamics of iSeroSnFR (left) and GFP (right) activity during waking, NREM, and REM episodes (data from B, left) across time, normalized from onset to offset. Statistical comparisons of fluorescence levels were performed on the last 10% of data within each behavioral state (one-way ANOVA with Bonferroni correction).

(D) Single-trial or averaged fluorescence change across all trials of iSeroSnFR from NREM to wake, REM to wake, wake to NREM, and NREM to REM transitions. Statistical comparisons of changes in fluorescence using and BLA^{iSeroSnFR} were made based on the average fluorescence over 15 s before and 15 s after the behavioral state transition. N = 15 trials/animal, n = 3 BLA^{GFP}, and n = 9 BLA^{iSeroSnFR}. Data represent mean \pm SEM. ***p < 0.001, paired Student's t test.

See also Figure S7.

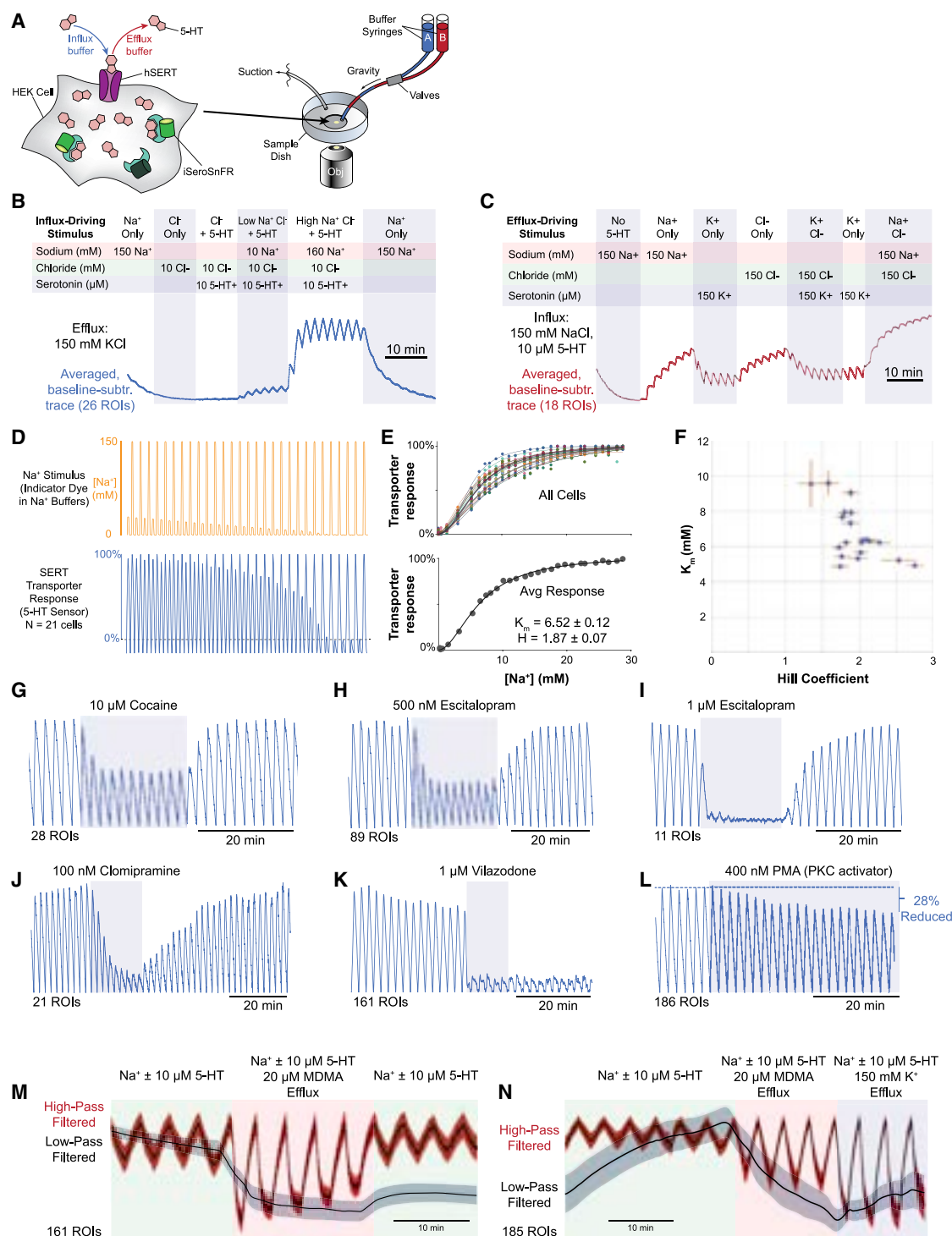


Figure 6. Application to Monitoring hSERT Transport

(A) Schematic of the oscillating stimulus transporter assay (OSTA).

(B) Confirmation of ionic requirements of hSERT for 5-HT uptake: influx only occurs in the presence of 5-HT, Na⁺, and Cl⁻.

(C) Ions driving hSERT-mediated 5-HT efflux: rates of efflux increase with K⁺ and are insensitive to Cl⁻.

(D–F) Sodium dependence of 5-HT transport through hSERT.

(D) Cells were subjected to a decreasing linear gradient of Na⁺ in the influx buffer, with standardized “fiducial” bouts at saturating sodium concentration interleaved. Red fluorescence (sulforhodamine 101 at 200 nM in fiducials) was used as a readout for the sodium stimulus (top panel), and green fluorescence (iSeroSnFR) reflected changes in cytosolic [5-HT] due to hSERT function (bottom panel).

(legend continued on next page)

(Bermingham and Blakely, 2016). Since the decrement was relatively slow, it is likely that it represents extraction of transporters from cell membranes, also consistent with literature (Bermingham and Blakely, 2016).

Finally, we examined pharmacologically driven efflux of 5-HT, which has been proposed to underlie the psychoactive effects of psychedelics such as 3,4-methyl enedioxy methamphetamine (MDMA, “ecstasy”; acting mainly via SERT) (Rudnick and Sandtner, 2019). We omitted KCl from the efflux buffer, so oscillations were instead driven solely by presence or absence of 5-HT (0 or 10 μ M). 20 μ M MDMA was then added to the 5-HT-free buffer to probe its capacity for driving 5-HT efflux. We observed a 2-fold enhancement in efflux in the presence of 20 μ M MDMA (Figure 6M). The ratio of efflux magnitude was about 1:2:3 for Na⁺-, MDMA-, and K⁺-driven effluxes, respectively (Figure 6N). The smaller magnitude of efflux driven by 5-HT removal alone results from the ability of extracellular Na⁺ to stabilize hSERT in an outward-facing conformation, thereby slowing down reverse transport (Zhang et al., 2016). MDMA-driven efflux probably reflects a different process in which hSERT catalyzes exchange of intracellular 5-HT with extracellular MDMA, without utilizing the entire transport cycle (Rudnick and Wall, 1992). As a whole, these experiments show that iSeroSnFR coupled with OSTA is a powerful tool for rapid, precise pharmacological characterization.

DISCUSSION

Use of Machine Learning to Accelerate Directed Evolution

Our combined Rosetta and machine-learning-guided directed evolution approach was quite effective. After just one round of each, we screened fewer than 2,600 variants, but made dramatic improvements to the sensor’s affinity, specificity, and fluorescence response. After just two more rounds of machine-learning-guided directed evolution, we had screened a total of ~16,000 variants, interrogated more than 60 different protein scaffold positions, and introduced 19 mutations into our final sensor, increasing its 5-HT affinity by >5,000-fold, abolishing choline/ACh binding, and increasing fluorescence response by 3-fold compared to the starting scaffold, iAChSnFR0.6. The efficacy of the design cycle diminished somewhat with each round. However, these results validate the rankings of the initial RF model, which predicted high impacts for the top 4 positions and progressively lower impacts for each successive position. Nonetheless, in each round, the best variant came from the GLM-predicted library; in rounds 1 and 2, these variants were nearly twice as good as the best-performing variant from the SSM library. Because RF uses an ensemble method, we could identify the most important features (protein positions) and provide guidance for subsequent stages. GLM is a good classifier even for small (<10,000) training datasets and is ideal for first-pass data analysis (Yang et al., 2019a). Our entire dataset was used for

training (no test data), because our models were used only to guide one round of library design at a time.

Headroom remains in the iSeroSnFR scaffold, particularly for higher-affinity versions for better detection of sparse signaling events. It is likely that the machine-learning-guided approach detailed here can produce further gains, although each round thus far produced diminishing returns. A high-resolution structure of ligand-bound iSeroSnFR could reinvigorate this process, but we have been as yet unable to obtain such a structure. Alternatively, the addition of more biophysical parameters to the model, or more advanced ML models such as universal transformers (Dehghani et al., 2019), Bayesian optimization (Yang et al., 2019b), or neural networks (Kato et al., 2005), could extract sequence/function relationships that we missed. On a related note, it will be broadly useful for the field to somehow incorporate ML-gleaned insights back into the biophysical potential functions underlying structure-based computational protein design. Regardless, the method described here was highly effective for our purposes, and we expect that it can be used to engineer other PBP-based neuromodulator sensors, and more generally to tackle other challenging protein-engineering tasks.

Molecular Properties of iSeroSnFR

iSeroSnFR is highly selective for 5-HT over other endogenous signaling molecules and drugs (Figures 2C and S3). The physiological concentration of 5-HT has been estimated using FSCV to be in the high-nM to low- μ M range (Bunin and Wightman, 1998; Bunin et al., 1998). The functional affinity of iSeroSnFR is in the high- μ M range, much larger than endogenous monoamine receptors. However, its very large fluorescence response ($\Delta F/F_0$)_{max}, which is 3- to 30-fold larger than that of GPCR-based sensors (Jing et al., 2019; Mizuno et al., 2019; Wan et al., 2020), means that low concentrations are still readily detectable. On mammalian cells, iSeroSnFR reliably detected concentrations as low as ~350 pM (Figures 2F and S4B). Indeed, this high dynamic range and weaker affinity offers the additional advantages of fast kinetics (Helassa et al., 2018; Marvin et al., 2018) and low 5-HT buffering potential. Furthermore, the bio-orthogonal nature of the sensor reduces concerns of interference with endogenous receptors due to sensor overexpression. We have shown that the kinetics of iSeroSnFR are in the low millisecond range, both by stopped-flow (Figures 3D–3F) and by uncaging (Figures 3I–3K). We calculated both slow and fast components of the on-kinetics in purified protein, also observed with iGABASnFR and iGluSnFR (Marvin et al., 2019). Further investigation is needed to determine the mechanism underlying the apparently two-component on-kinetics. Nonetheless, we were able to demonstrate robust *in vivo* detection of millisecond-level release events. We believe that two-component on-kinetics could potentially serve as an advantage, in that the sensor could rapidly report lower concentration events, and then slowly read out larger changes in baseline occurring over several seconds. A higher-affinity sensor would quickly max out after low

(E) Fits of single-cell (top) and grouped (bottom) 5-HT transport responses to the stimulus shown in (D).

(F) Scatterplot of fitted parameters for individual cells: Hill coefficient versus K_m .

(G–L) hSERT-mediated 5-HT transport responses to various pharmacological agents (as indicated) under a standardized stimulus.

(M and N) MDMA-mediated 5-HT efflux: MDMA at 20 μ M in the efflux buffer significantly increased the rate of 5-HT efflux compared to Na⁺ alone. (N) In the last epoch of the experiment, K⁺ was substituted for Na⁺ in the efflux buffer for comparison to other experiments.

concentration events, and miss larger changes in baseline. However, the sensor is not without its limitations, and low concentration events might still be missed. Future engineering efforts will focus on producing a complementary sensor with higher affinity such that both high and low concentration events can be detected.

Imaging Endogenous 5-HT Release *Ex Vivo* and *In Vivo*

With iSeroSnFR, we replicated several salient biological results using photometry, with much higher temporal resolution than previously possible. We detected electrically evoked release, which was blocked by TTX. Surprisingly, we could not perturb observed fluorescent transients using blockers for SERT such as cocaine or citalopram, nor by the VMAT inhibitor reserpine. We expected cocaine and citalopram to prolong the 5-HT transients measured in slice by inhibiting 5-HT reuptake, as we showed *in vitro* (Figure 6G). Given the fast off-kinetics (Figures 3K and 3L), it is unlikely that sensor unbinding dominates the response waveform and obscures drug effects. Alternatively, in the brain slice preparation, released 5-HT potentially diffuses away, with SERT playing a minimal role in observed waveforms. Although possible, this is unlikely, given previous results using FSCV (Matsui and Alvarez, 2018). However, other groups have seen similar negative results, e.g., the inability of the SERT blocker fluoxetine to affect electrical stimulation-evoked 5-HT release amplitude and kinetics in the mouse dorsal raphe nucleus (Bunin and Wightman, 1998). It is also unclear why inhibition of VMAT with reserpine failed to block the transients by depleting 5-HT storage in synaptic vesicles. It is possible that reserpine only slowly depletes 5-HT from vesicles in brain slice. We also noticed that the apparent affinity in slice is right-shifted from that in dissociated neuronal culture. This is not unexpected, given the added confounds of tissue penetration for bath applied 5-HT and dilution of micropipetted 5-HT in the slice environment, which do not exist in monolayered cultured cells. Reassuringly, the successful *in vivo* detection of endogenously released 5-HT suggests that this reflects an artifact of the slice preparation in this context and not a true weakening of affinity following long-term expression. Future experiments will focus on direct comparison with FSCV and microdialysis to further characterize the properties—and deficiencies—of the sensor.

Our *in vivo* studies very clearly show functionality of the sensor across multiple brain regions and multiple behaviors, across both short and long time windows. iSeroSnFR signals are consistent with 5-HT microdialysis studies in fear conditioning in both BLA and mPFC (Ferrés-Coy et al., 2013; Forster et al., 2006; Fujino et al., 2002; Hashimoto et al., 1999; Kawahara et al., 1993; Rueter and Jacobs, 1996; Yokoyama et al., 2005), but offer much improved temporal resolution, indicating that iSeroSnFR is a viable alternative to these techniques. iSeroSnFR revealed obvious 5-HT increases in mPFC and BLA during cued fear conditioning, consistent with previous studies (Bauer, 2015). OFC responds robustly to social interaction (Figure S6I), and it is clear that serotonergic input to frontal cortex and other brain regions is complex and heterogeneous. The high sensitivity and millisecond-level temporal resolution of iSeroSnFR will be instrumental in working out such details. Furthermore, the causes and consequences of endogenous 5-HT release, and how closely optogenetically triggered release mimics it, remain uncertain (Correia et al., 2017; Garcia-Garcia et al., 2018; Marcinkiewicz

et al., 2016; Ohmura et al., 2014; Seo et al., 2019). *In vivo* recording in target brain regions using iSeroSnFR will provide new opportunities to study 5-HT modulation by electrical, opto/chemogenetic, or behavioral manipulations, 5-HT interaction with other neurotransmitters such as glutamate or dopamine, and 5-HT function in the context of various behavioral states.

For initial *in vivo* demonstration of iSeroSnFR, we opted for fiber photometry, a simple and widely used technique. We replicated published FSCV results as a proof-of-principle, in multiple behavioral paradigms, across multiple brain regions. This technique, however, does not demonstrate the full potential of optical sensors, because essentially all spatial resolution is lost. *In vivo* two-photon imaging is the gold standard for high-resolution tracking of neural signaling in intact animals. iSeroSnFR is completely compatible with two-photon imaging, as we have demonstrated in brain slice (Figures S5B–S5F). Its spectral and biophysical properties are similar to that of iGluSnFR and GCaMP, routinely used in *in vivo* two-photon imaging. We thus anticipate no sensor-specific challenges for *in vivo* two-photon iSeroSnFR imaging in diverse preparations.

Finally, while we have demonstrated the uses of iSeroSnFR for several neuroscience applications, the vast majority of 5-HT is produced in the gut, and indeed 5-HT receptors exist throughout the body. Studies of 5-HT in peripheral systems would be exciting and informative, and we expect that iSeroSnFR could be adapted for these purposes.

Screening 5-HT Transporter Modulators

The soluble nature of iSeroSnFR provides an additional advantage over the use of integral-membrane GPCR-based scaffolds. The excellent dynamic range of the sensor, combined with its robust cytoplasmic expression, allowed us to easily monitor time-resolved kinetics of 5-HT influx and efflux, and how transport is distinctly modulated by various drugs, including two drugs of abuse and three antidepressants. GPCR-based sensors would be incompatible with this application, because they cannot be expressed cytoplasmically, and GPCRs respond directly to many of the very drugs such an assay is designed to characterize. iSeroSnFR, on the other hand, is far more specific, allowing these critical pharmacological experiments. Given the clinical significance of hSERT and its mutants in psychological disorders (Jarrett et al., 2007; Margoob and Mushtaq, 2011; Ozaki et al., 2003; Wankler et al., 2014), this assay will greatly facilitate serotonergic drug discovery by identifying and quantifying the underlying properties of drug-hSERT interactions, paving the way for screening patient-specific drugs and doses for SSRIs or other drugs.

STAR★METHODS

Detailed methods are provided in the online version of this paper and include the following:

- KEY RESOURCES TABLE
- RESOURCE AVAILABILITY
 - Lead Contact
 - Materials Availability
 - Data and Code Availability
- EXPERIMENTAL MODEL AND SUBJECT DETAILS

- Mice and Rats
- **METHOD DETAILS**
 - Methods specific to luciferase
 - Construction of luciferase library and mutants
 - Primer lists
 - General bioluminescence imaging protocol
 - Lysate screening of combination library
 - Methods specific to iSeroSnFR
 - Design.options
 - Backrub.options
 - Backrub.bash
 - Design.xml
 - Cloning
 - Library generation
 - Library screening
 - Protein purification
 - Specificity screening
 - Crystallization and data collection
 - Protein Sequences
 - Tissue Culture
 - Dissociated hippocampal neuronal culture
 - Dose-response curves
 - Stopped-flow
 - Uncaging
 - Virus production
 - Surgical procedures for slice experiments
 - Brain slices for 2-photon imaging
 - Brain slices for 1-photon photometry
 - Surgical procedures for *in vivo* mouse experiments
 - Viral injection
 - Optical fiber implantation
 - EEG and EMG implantation
 - Histology
 - Immunohistochemistry
 - Fiber photometry
 - Polysomnographic recordings
 - Sleep/wake analysis
 - Fear conditioning
 - Running wheels
 - Free Social Interaction
 - Oscillating Stimulus Transporter Assay
- **QUANTIFICATION AND STATISTICAL ANALYSIS**
 - Image analysis
 - Fiber photometry
 - EEG spectrogram
 - Statistical methods

SUPPLEMENTAL INFORMATION

Supplemental Information can be found online at <https://doi.org/10.1016/j.cell.2020.11.040>.

ACKNOWLEDGMENTS

We would like to thank Drs. Liqun Luo (Stanford University) and Jing Ren (MRC) for their critical reading and feedback. This work is based upon research conducted at the Northeastern Collaborative Access Team beamlines, which are funded by the National Institute of General Medical Sciences from the NIH (P30-GM124165). The Pilatus 6M detector on the 24-ID-C beamline is funded

by an NIH-ORIP HEI grant (S10-RR029205). This research used resources of the Advanced Photon Source, a US Department of Energy (DOE) Office of Science User Facility operated for the DOE Office of Science by Argonne National Laboratory under contract DE-AC02-06CH11357. This work was supported by funding to L.T. (BRAIN Initiative U01NS090604, U01NS013522, and DP2MH107056 from NIH), to E.K.U. (Mistletoe Foundation Research Fellowship), and to G.O.M. (ARCS Scholarship), as well as by the Howard Hughes Medical Institute. V.G. is a Heritage Principal Investigator supported by the Heritage Medical Research Institute, the NIH (BRAIN RF1MH117069), the Center for Molecular and Cellular Neuroscience of the Chen Institute, and the Beckman Institute for CLARITY, Optogenetics and Vector Engineering Research. V.A.A. is funded by Intramural Programs of NIAAA and NINDS ZIA-AA000421 and Innovation Award from NIH-DDIR. T.L.K. is funded by the NIH (R01AA019454, P60AA011605, and U24AA025475), and O.J.H. is funded by the NIH (5T32NS007431-20).

AUTHOR CONTRIBUTIONS

E.K.U., J.P.K., M.A., L.L.L., and L.T. conceived of and designed the study. E.K.U. designed the machine-learning method, screened and optimized sensors, and characterized them in purified protein, mammalian cells, cultured neurons, and brain slice, with significant contribution from C.D., D.A.J., and J.S. J.P.K., S.S., and G.R. designed OSTA and stopped-flow experiments, and J.P.K. performed them. M.A. and V.G. designed and performed *in vivo* fiber photometry and EEG/EMG recording in BLA and mPFC in fear learning and sleep/wake cycles. O.J.H., M.E.F., and T.L.K. designed and performed *in vivo* fiber photometry experiments in BLA, OFC, and BNST during social interaction. R.L. and V.Y.-Y. designed and performed computational Rosetta modeling. Z.Y. and J.A.P. provided luciferase experimental data for establishing machine-learning methods. J.C. and D.T.L. provided significant insight for the machine-learning methods. J.S. characterized the sensor in acute slice using two-photon imaging. A.M. and V.A.A. designed and performed photometry imaging in acute slice. S.H. and A.J.F. performed crystallography. J.S.M., P.M.B., A.V.S., H.A.L., and L.L.L. provided iAChSnFR0.6 and performed preliminary experiments on serotonin binding. S.B. and L.D.L. synthesized caged serotonin. G.O.M. provided dissociated neuronal cultures. L.P.C. and D.E.O. produced chemical reagents. S.M.U. and S.G.A. provided SSRIs and guidance in cell-assay design. E.K.U., J.P.K., L.L.L., and L.T. wrote the manuscript with significant input from other authors.

DECLARATION OF INTERESTS

L.T. and G.O.M. are co-founders of Seven Biosciences. D.E.O. is a founder of Delix.

Received: November 23, 2019

Revised: June 22, 2020

Accepted: November 20, 2020

Published: December 16, 2020

REFERENCES

- Abdalla, A., Atcherley, C.W., Pathirathna, P., Samaranayake, S., Qiang, B., Peña, E., Morgan, S.L., Heien, M.L., and Hashemi, P. (2017). In Vivo Ambient Serotonin Measurements at Carbon-Fiber Microelectrodes. *Anal. Chem.* 89, 9703–9711.
- Baker, D. (2019). What has de novo protein design taught us about protein folding and biophysics? *Protein Sci.* 28, 678–683.
- Bang, S.J., Jensen, P., Dymecki, S.M., and Commons, K.G. (2012). Projections and interconnections of genetically defined serotonin neurons in mice. *Eur. J. Neurosci.* 35, 85–96.
- Bauer, E.P. (2015). Serotonin in fear conditioning processes. *Behav. Brain Res.* 277, 68–77.
- Bedbrook, C.N., Yang, K.K., Robinson, J.E., Gradinaru, V., and Arnold, F.H. (2019). Machine learning-guided channelrhodopsin engineering enables minimally-invasive optogenetics. *bioRxiv*. <https://doi.org/10.1101/565606>.

- Belmaker, R.H., and Agam, G. (2008). Major depressive disorder. *N. Engl. J. Med.* 358, 55–68.
- Belmer, A., Klenowski, P.M., Patkar, O.L., and Bartlett, S.E. (2017). Mapping the connectivity of serotonin transporter immunoreactive axons to excitatory and inhibitory neurochemical synapses in the mouse limbic brain. *Brain Struct. Funct.* 222, 1297–1314.
- Bender, B.J., Cisneros, A., 3rd, Duran, A.M., Finn, J.A., Fu, D., Lokits, A.D., Mueller, B.K., Sangha, A.K., Sauer, M.F., Sevy, A.M., et al. (2016). Protocols for Molecular Modeling with Rosetta3 and RosettaScripts. *Biochemistry* 55, 4748–4763.
- Berger, M., Gray, J.A., and Roth, B.L. (2009). The expanded biology of serotonin. *Annu. Rev. Med.* 60, 355–366.
- Bermingham, D.P., and Blakely, R.D. (2016). Kinase-dependent Regulation of Monoamine Neurotransmitter Transporters. *Pharmacol. Rev.* 68, 888–953.
- Besette, P.H., Mena, M.A., Nguyen, A.W., and Daugherty, P.S. (2003). Construction of designed protein libraries using gene assembly mutagenesis. *Methods Mol. Biol.* 231, 29–37.
- Biswas, S., Kuznetsov, G., Ogden, P.J., Conway, N.J., Adams, R.P., and Church, G.M. (2018). Toward machine-guided design of proteins. *bioRxiv*. <https://doi.org/10.1101/337154>.
- Bocchio, M., McHugh, S.B., Bannerman, D.M., Sharp, T., and Capogna, M. (2016). Serotonin, Amygdala and Fear: Assembling the Puzzle. *Front. Neural Circuits* 10, 24.
- Borden, P.M., Zhang, P., Shivange, A.V., Marvin, J.S., Cichon, J., Dan, C., Podgorski, K., Figueiredo, A., Novak, O., Tanimoto, M., et al. (2020). A fast genetically encoded fluorescent sensor for faithful in vivo acetylcholine detection in mice, fish, worms and flies. *bioRxiv*. <https://doi.org/10.1101/2020.02.07.939504>.
- Bos, N., Dreier, S., Jørgensen, C.G., Nielsen, J., Guerrieri, F.J., and d'Ettorre, P. (2012). Learning and perceptual similarity among cuticular hydrocarbons in ants. *J. Insect Physiol.* 58, 138–146.
- Breiman, L. (2001). Breiman and Cutler's Random Forests for Classification and Regression. *Mach. Learn.* 45, 5–32.
- Broussard, G.J., Liang, R., and Tian, L. (2014). Monitoring activity in neural circuits with genetically encoded indicators. *Front. Mol. Neurosci.* 7, 97.
- Broussard, G.J., Unger, E.K., Liang, R., McGrew, B.P., and Tian, L. (2018). Imaging glutamate with genetically encoded fluorescent sensors. In *Biochemical Approaches for Glutamatergic Neurotransmission*, S. Parrot and L. Denoroy, eds. (Springer New York), pp. 117–153.
- Bryksin, A.V., and Matsumura, I. (2010). Overlap extension PCR cloning: a simple and reliable way to create recombinant plasmids. *Biotechniques* 48, 463–465.
- Bunin, M.A., and Wightman, R.M. (1998). Quantitative evaluation of 5-hydroxytryptamine (serotonin) neuronal release and uptake: an investigation of extra-synaptic transmission. *J. Neurosci.* 18, 4854–4860.
- Bunin, M.A., Prileau, C., Mailman, R.B., and Wightman, R.M. (1998). Release and uptake rates of 5-hydroxytryptamine in the dorsal raphe and substantia nigra reticulata of the rat brain. *J. Neurochem.* 70, 1077–1087.
- Burghardt, N.S., Bush, D.E.A., McEwen, B.S., and LeDoux, J.E. (2007). Acute selective serotonin reuptake inhibitors increase conditioned fear expression: blockade with a 5-HT_{2C} receptor antagonist. *Biol. Psychiatry* 62, 1111–1118.
- Calhoon, G.G., and Tye, K.M. (2015). Resolving the neural circuits of anxiety. *Nat. Neurosci.* 18, 1394–1404.
- Charnay, Y., and Léger, L. (2010). Brain serotonergic circuitries. *Dialogues Clin. Neurosci.* 12, 471–487.
- Chen, V.B., Arendall, W.B., 3rd, Headd, J.J., Keedy, D.A., Immormino, R.M., Kapral, G.J., Murray, L.W., Richardson, J.S., and Richardson, D.C. (2010). MolProbity: all-atom structure validation for macromolecular crystallography. *Acta Crystallogr. D Biol. Crystallogr.* 66, 12–21.
- Cho, J.R., Treweek, J.B., Robinson, J.E., Xiao, C., Bremner, L.R., Greenbaum, A., and Gradinaru, V. (2017). Dorsal Raphe Dopamine Neurons Modulate Arousal and Promote Wakefulness by Salient Stimuli. *Neuron* 94, 1205–1219.
- Cipriani, A., Furukawa, T.A., Salanti, G., Chaimani, A., Atkinson, L.Z., Ogawa, Y., Leucht, S., Ruhe, H.G., Turner, E.H., Higgins, J.P.T., et al. (2018). Comparative efficacy and acceptability of 21 antidepressant drugs for the acute treatment of adults with major depressive disorder: a systematic review and network meta-analysis. *Lancet* 391, 1357–1366.
- Clarke, R.J., and Khalid, M.A.A. (2015). Pumps, Channels and Transporters: Methods of Functional Analysis (John Wiley & Sons).
- Cobb, R.E., Chao, R., and Zhao, H. (2013). Directed Evolution: Past, Present and Future. *AIChE J.* 59, 1432–1440.
- Correia, J., van Zessen, R., and Pascoli, V. (2018). Dopamine neurons projecting to medial shell of the nucleus accumbens drive heroin reinforcement. *eLife* 7, e39945.
- Correia, P.A., Lottem, E., Banerjee, D., Machado, A.S., Carey, M.R., and Mainen, Z.F. (2017). Transient inhibition and long-term facilitation of locomotion by phasic optogenetic activation of serotonin neurons. *eLife* 6, e20975.
- Curzon, P., Rustay, N.R., and Browman, K.E. (2009). Cued and contextual fear conditioning for rodents. In *Methods of Behavior Analysis in Neuroscience*, J.J. Buccafusco, ed. (CRC Press/Taylor & Francis).
- Davis, I.W., and Baker, D. (2009). RosettaLigand docking with full ligand and receptor flexibility. *J. Mol. Biol.* 385, 381–392.
- Dehghani, M., Gouws, S., Vinyals, O., Uszkoreit, J., and Kaiser, L. (2019). Universal Transformers (ICLR).
- Dobson, A.J., Barnett, A.G., and Barnett, A.G. (2008). An Introduction to Generalized Linear Models (Chapman and Hall/CRC).
- Ehren, J., Govindarajan, S., Morón, B., Minshull, J., and Khosla, C. (2008). Protein engineering of improved prolyl endopeptidases for celiac sprue therapy. *Protein Eng. Des. Sel.* 21, 699–707.
- Emsley, P., and Cowtan, K. (2004). Coot: model-building tools for molecular graphics. *Acta Crystallogr. D Biol. Crystallogr.* 60, 2126–2132.
- Evans, P.R., and Murshudov, G.N. (2013). How good are my data and what is the resolution? *Acta Crystallogr. D Biol. Crystallogr.* 69, 1204–1214.
- Feng, J., Zhang, C., Lischinsky, J.E., Jing, M., Zhou, J., Wang, H., Zhang, Y., Dong, A., Wu, Z., Wu, H., et al. (2019). A Genetically Encoded Fluorescent Sensor for Rapid and Specific In Vivo Detection of Norepinephrine. *Neuron* 102, 745–761.
- Ferrés-Coy, A., Pilar-Cuellar, F., Vidal, R., Paz, V., Masana, M., Cortés, R., Carmona, M.C., Campa, L., Pazos, A., Montefeltro, A., et al. (2013). RNAi-mediated serotonin transporter suppression rapidly increases serotonergic neurotransmission and hippocampal neurogenesis. *Transl. Psychiatry* 3, e211.
- Forster, G.L., Feng, N., Watt, M.J., Korzan, W.J., Mouw, N.J., Summers, C.H., and Renner, K.J. (2006). Corticotropin-releasing factor in the dorsal raphe elicits temporally distinct serotonergic responses in the limbic system in relation to fear behavior. *Neuroscience* 141, 1047–1055.
- Fujino, K., Yoshitake, T., Inoue, O., Ibi, N., Kehr, J., Ishida, J., Nohta, H., and Yamaguchi, M. (2002). Increased serotonin release in mice frontal cortex and hippocampus induced by acute physiological stressors. *Neurosci. Lett.* 320, 91–95.
- García-García, A.L., Canetta, S., Stujenske, J.M., Burghardt, N.S., Ansorge, M.S., Dranovsky, A., and Leonardo, E.D. (2018). Serotonin inputs to the dorsal BNST modulate anxiety in a 5-HT_{1A} receptor-dependent manner. *Mol. Psychiatry* 23, 1990–1997.
- Gibson, D.G., Young, L., Chuang, R.-Y., Venter, J.C., Hutchison, C.A., 3rd, and Smith, H.O. (2009). Enzymatic assembly of DNA molecules up to several hundred kilobases. *Nat. Methods* 6, 343–345.
- Gong, S., Zheng, C., Doughty, M.L., Losos, K., Didkovsky, N., Schambra, U.B., Nowak, N.J., Joyner, A., Leblanc, G., Hatten, M.E., et al. (2003). A gene expression atlas of the central nervous system based on bacterial artificial chromosomes. *Nature* 425, 917–925.
- Greenwood, B.N., Foley, T.E., Day, H.E.W., Burhans, D., Brooks, L., Campeau, S., and Fleshner, M. (2005). Wheel running alters serotonin (5-HT) transporter, 5-HT_{1A}, 5-HT_{1B}, and alpha 1b-adrenergic receptor mRNA in the rat raphe nuclei. *Biol. Psychiatry* 57, 559–568.

- Hashimoto, S., Inoue, T., and Koyama, T. (1999). Effects of conditioned fear stress on serotonin neurotransmission and freezing behavior in rats. *Eur. J. Pharmacol.* 378, 23–30.
- Hawkins, P.C.D., Skillman, A.G., Warren, G.L., Ellingson, B.A., and Stahl, M.T. (2010). Conformer generation with OMEGA: algorithm and validation using high quality structures from the Protein Databank and Cambridge Structural Database. *J. Chem. Inf. Model.* 50, 572–584.
- Heinrich, T., Böttcher, H., Gericke, R., Bartoszyk, G.D., Anzali, S., Seyfried, C.A., Greiner, H.E., and Van Amsterdam, C. (2004). Synthesis and structure-activity relationship in a class of indolebutylpiperazines as dual 5-HT(1A) receptor agonists and serotonin reuptake inhibitors. *J. Med. Chem.* 47, 4684–4692.
- Helassa, N., Dürst, C.D., Coates, C., Kerruth, S., Arif, U., Schulze, C., Wiegert, J.S., Geeves, M., Oertner, T.G., and Török, K. (2018). Ultrafast glutamate sensors resolve high-frequency release at Schaffer collateral synapses. *Proc. Natl. Acad. Sci. USA* 115, 5594–5599.
- Huang, R., Fang, P., and Kay, B.K. (2012). Improvements to the Kunkel mutagenesis protocol for constructing primary and secondary phage-display libraries. *Methods* 58, 10–17.
- Jaquins-Gerstl, A., and Michael, A.C. (2015). A review of the effects of FSCV and microdialysis measurements on dopamine release in the surrounding tissue. *Analyst (Lond.)* 140, 3696–3708.
- Jarrett, M.E., Kohen, R., Cain, K.C., Burr, R.L., Poppe, A., Navaja, G.P., and Heitkemper, M.M. (2007). Relationship of SERT polymorphisms to depressive and anxiety symptoms in irritable bowel syndrome. *Biol. Res. Nurs.* 9, 161–169.
- Jing, M., Zhang, Y., Wang, H., and Li, Y. (2019). G-protein-coupled receptor-based sensors for imaging neurochemicals with high sensitivity and specificity. *J. Neurochem.* 151, 279–288.
- Jing, M., Li, Y., Zeng, J., Huang, P., Skirzewski, M., Kijakic, O., Peng, W., Qian, T., Tan, K., Zou, J., et al. (2020). An optimized acetylcholine sensor for monitoring in vivo cholinergic activity. *Nat. Methods* 17, 1139–1146.
- Jones, K.A., Porterfield, W.B., Rathbun, C.M., McCutcheon, D.C., Paley, M.A., and Prescher, J.A. (2017). Orthogonal Luciferase-Luciferin Pairs for Bioluminescence Imaging. *J. Am. Chem. Soc.* 139, 2351–2358.
- Kabsch, W. (2010). XDS. *Acta Crystallogr. D Biol. Crystallogr.* 66, 125–132.
- Kato, R., Nakano, H., Konishi, H., Kato, K., Koga, Y., Yamane, T., Kobayashi, T., and Honda, H. (2005). Novel strategy for protein exploration: high-throughput screening assisted with fuzzy neural network. *J. Mol. Biol.* 351, 683–692.
- Kawahara, H., Yoshida, M., Yokoo, H., Nishi, M., and Tanaka, M. (1993). Psychological stress increases serotonin release in the rat amygdala and prefrontal cortex assessed by in vivo microdialysis. *Neurosci. Lett.* 162, 81–84.
- Keller, J.P., and Looger, L.L. (2016). The Oscillating Stimulus Transporter Assay, OSTA: Quantitative Functional Imaging of Transporter Protein Activity in Time and Frequency Domains. *Mol. Cell* 64, 199–212.
- Keller, J.P., Marvin, J.S., Lacin, H., Lemon, W.C., Shea, J., Kim, S., Lee, R.T., Koyama, M., Keller, P.J., and Looger, L.L. (2019). In vivo glucose imaging in multiple model organisms with an engineered single-wavelength sensor. *bioRxiv*. <https://doi.org/10.1101/571422>.
- Khoury, G.A., Smadbeck, J., Kieslich, C.A., and Floudas, C.A. (2014). Protein folding and de novo protein design for biotechnological applications. *Trends Biotechnol.* 32, 99–109.
- Kiser, D., Steemers, B., Branchi, I., and Homberg, J.R. (2012). The reciprocal interaction between serotonin and social behaviour. *Neurosci Biobehav Rev* 36, 786–798.
- Koldso, H., Noer, P., Grouleff, J., Autzen, H.E., Sinning, S., and Schjøtt, B. (2011). Unbiased simulations reveal the inward-facing conformation of the human serotonin transporter and Na(+) ion release. *PLoS Comput. Biol.* 7, e1002246.
- Kunkel, T.A. (1985). Rapid and efficient site-specific mutagenesis without phenotypic selection. *Proc. Natl. Acad. Sci. USA* 82, 488–492.
- Li, Y., Zhong, W., Wang, D., Feng, Q., Liu, Z., Zhou, J., Jia, C., Hu, F., Zeng, J., Guo, Q., et al. (2016). Serotonin neurons in the dorsal raphe nucleus encode reward signals. *Nat. Commun.* 7, 10503.
- Liao, J., Warmuth, M.K., Govindarajan, S., Ness, J.E., Wang, R.P., Gustafsson, C., and Minshull, J. (2007). Engineering proteinase K using machine learning and synthetic genes. *BMC Biotechnol.* 7, 16.
- Liaw, A., and Wiener, M. (2002). Classification and Regression by randomForest. <https://rdrr.io/cran/randomForest/>.
- Lin, M.Z., and Schnitzer, M.J. (2016). Genetically encoded indicators of neuronal activity. *Nat. Neurosci.* 19, 1142–1153.
- Lobas, M.A., Tao, R., Nagai, J., Kronschräger, M.T., Borden, P.M., Marvin, J.S., Looger, L.L., and Khakh, B.S. (2019). A genetically encoded single-wavelength sensor for imaging cytosolic and cell surface ATP. *Nat. Commun.* 10, 711.
- Looger, L.L., and Griesbeck, O. (2012). Genetically encoded neural activity indicators. *Curr. Opin. Neurobiol.* 22, 18–23.
- Madisen, L., Zwingman, T.A., Sunkin, S.M., Oh, S.W., Zariwala, H.A., Gu, H., Ng, L.L., Palmiter, R.D., Hawrylycz, M.J., Jones, A.R., et al. (2010). A robust and high-throughput Cre reporting and characterization system for the whole mouse brain. *Nat. Neurosci.* 13, 133–140.
- Madisen, L., Garner, A.R., Shimaoka, D., Chuong, A.S., Klapoetke, N.C., Li, L., van der Bourg, A., Niino, Y., Ego, L., Monetti, C., et al. (2015). Transgenic mice for intersectional targeting of neural sensors and effectors with high specificity and performance. *Neuron* 85, 942–958.
- Marcinkiewicz, C.A., Mazzone, C.M., D’Agostino, G., Halladay, L.R., Hardaway, J.A., DiBerto, J.F., Navarro, M., Burnham, N., Cristiano, C., Dorrier, C.E., et al. (2016). Serotonin engages an anxiety and fear-promoting circuit in the extended amygdala. *Nature* 537, 97–101.
- Margoob, M.A., and Mushtaq, D. (2011). Serotonin transporter gene polymorphism and psychiatric disorders: is there a link? *Indian J. Psychiatry* 53, 289–299.
- Marvin, J.S., Schreiter, E.R., Echevarría, I.M., and Looger, L.L. (2011). A genetically encoded, high-signal-to-noise maltose sensor. *Proteins* 79, 3025–3036.
- Marvin, J.S., Borghuis, B.G., Tian, L., Cichon, J., Harnett, M.T., Akerboom, J., Gordus, A., Renninger, S.L., Chen, T.-W., Bargmann, C.I., et al. (2013). An optimized fluorescent probe for visualizing glutamate neurotransmission. *Nat. Methods* 10, 162–170.
- Marvin, J.S., Scholl, B., Wilson, D.E., Podgorski, K., Kazempour, A., Müller, J.A., Schoch, S., Quiroz, F.J.U., Rebola, N., Bao, H., et al. (2018). Stability, affinity, and chromatic variants of the glutamate sensor iGluSnFR. *Nat. Methods* 15, 936–939.
- Marvin, J.S., Shimoda, Y., Magloire, V., Leite, M., Kawashima, T., Jensen, T.P., Kolb, I., Knott, E.L., Novak, O., Podgorski, K., et al. (2019). A genetically encoded fluorescent sensor for in vivo imaging of GABA. *Nat. Methods* 16, 763–770.
- Matsui, A., and Alvarez, V.A. (2018). Cocaine Inhibition of Synaptic Transmission in the Ventral Pallidum Is Pathway-Specific and Mediated by Serotonin. *Cell Rep.* 23, 3852–3863.
- McCoy, A.J. (2007). Solving structures of protein complexes by molecular replacement with Phaser. *Acta Crystallogr. D Biol. Crystallogr.* 63, 32–41.
- Miller, D.A., Suen, G., Bruce, D., Copeland, A., Cheng, J.-F., Detter, C., Goodwin, L.A., Han, C.S., Hauser, L.J., Land, M.L., et al. (2011). Complete genome sequence of the cellulose-degrading bacterium *Cellulosilyticum lentocellum*. *J. Bacteriol.* 193, 2357–2358.
- Mizuno, G.O., Unger, E.K., and Tian, L. (2019). Real-time monitoring of neuro-modulators in behaving animals using genetically-encoded indicators. In *Compendium on In Vivo Monitoring in Real-Time Molecular Neuroscience*, G.S. Wilson and A.C. Michael, eds. (World Scientific), pp. 1–18.
- Nov, Y. (2012). When second best is good enough: another probabilistic look at saturation mutagenesis. *Appl. Environ. Microbiol.* 78, 258–262.
- Ohmura, Y., Tanaka, K.F., Tsunematsu, T., Yamanaka, A., and Yoshioka, M. (2014). Optogenetic activation of serotonergic neurons enhances anxiety-like behaviour in mice. *Int. J. Neuropsychopharmacol.* 17, 1777–1783.

- Ollikainen, N., de Jong, R.M., and Kortemme, T. (2015). Coupling Protein Side-Chain and Backbone Flexibility Improves the Re-design of Protein-Ligand Specificity. *PLoS Comput. Biol.* **11**, e1004335.
- Ozaki, N., Goldman, D., Kaye, W.H., Plotnicov, K., Greenberg, B.D., Lappalainen, J., Rudnick, G., and Murphy, D.L. (2003). Serotonin transporter missense mutation associated with a complex neuropsychiatric phenotype. *Mol. Psychiatry* **8**, 933–936.
- Packer, M.S., and Liu, D.R. (2015). Methods for the directed evolution of proteins. *Nat. Rev. Genet.* **16**, 379–394.
- Patriarchi, T., Cho, J.R., Merten, K., Howe, M.W., Marley, A., Xiong, W.-H., Folk, R.W., Broussard, G.J., Liang, R., Jang, M.J., et al. (2018). Ultrafast neuronal imaging of dopamine dynamics with designed genetically encoded sensors. *Science* **360**, eaat4422.
- Peñalva, R.G., Lancel, M., Flachskamm, C., Reul, J.M.H.M., Holsboer, F., and Linthorst, A.C.E. (2003). Effect of sleep and sleep deprivation on serotonergic neurotransmission in the hippocampus: a combined in vivo microdialysis/EEG study in rats. *Eur. J. Neurosci.* **17**, 1896–1906.
- Portas, C.M., Bjorvatn, B., and Ursin, R. (2000). Serotonin and the sleep/wake cycle: special emphasis on microdialysis studies. *Prog. Neurobiol.* **60**, 13–35.
- Quan, J., and Tian, J. (2011). Circular polymerase extension cloning for high-throughput cloning of complex and combinatorial DNA libraries. *Nat. Protoc.* **6**, 242–251.
- Rathbun, C.M., Porterfield, W.B., Jones, K.A., Sagoe, M.J., Reyes, M.R., Hua, C.T., and Prescher, J.A. (2017). Parallel Screening for Rapid Identification of Orthogonal Bioluminescent Tools. *ACS Cent. Sci.* **3**, 1254–1261.
- Ren, J., Friedmann, D., Xiong, J., Liu, C.D., Ferguson, B.R., Weerakkody, T., DeLoach, K.E., Ran, C., Pun, A., Sun, Y., et al. (2018). Anatomically Defined and Functionally Distinct Dorsal Raphe Serotonin Sub-systems. *Cell* **175**, 472–487.
- Richter, F., Leaver-Fay, A., Khare, S.D., Bjelic, S., and Baker, D. (2011). De novo enzyme design using Rosetta3. *PLoS ONE* **6**, e19230.
- Ritz, C., Baty, F., Streibig, J.C., and Gerhard, D. (2015). Dose-Response Analysis Using R. *PLoS ONE* **10**, e0146021.
- Rouillard, J.-M., Lee, W., Truan, G., Gao, X., Zhou, X., and Gulari, E. (2004). Gene2Oligo: oligonucleotide design for in vitro gene synthesis. *Nucleic Acids Res.* **32**, W176–80.
- Rudnick, G., and Sandtner, W. (2019). Serotonin transport in the 21st century. *J. Gen. Physiol.* **151**, 1248–1264.
- Rudnick, G., and Wall, S.C. (1992). p-Chloroamphetamine induces serotonin release through serotonin transporters. *Biochemistry* **31**, 6710–6718.
- Rueter, L.E., and Jacobs, B.L. (1996). A microdialysis examination of serotonin release in the rat forebrain induced by behavioral/environmental manipulations. *Brain Res.* **739**, 57–69.
- Saito, T., and Nakatsuji, N. (2001). Efficient gene transfer into the embryonic mouse brain using in vivo electroporation. *Dev. Biol.* **240**, 237–246.
- Schindelin, J., Arganda-Carreras, I., Frise, E., Kaynig, V., Longair, M., Pietzsch, T., Preibisch, S., Rueden, C., Saalfeld, S., Schmid, B., et al. (2012). Fiji: an open-source platform for biological-image analysis. *Nat. Methods* **9**, 676–682.
- Schultz, K.N., and Kennedy, R.T. (2008). Time-resolved microdialysis for in vivo neurochemical measurements and other applications. *Annu. Rev. Anal. Chem. (Palo Alto, Calif.)* **1**, 627–661.
- Seo, C., Guru, A., Jin, M., Ito, B., Sleezer, B.J., Ho, Y.-Y., Wang, E., Boada, C., Krupa, N.A., Kullakanda, D.S., et al. (2019). Intense threat switches dorsal raphe serotonin neurons to a paradoxical operational mode. *Science* **363**, 538–542.
- Shivange, A.V., Borden, P.M., Muthusamy, A.K., Nichols, A.L., Bera, K., Bao, H., Bishara, I., Jeon, J., Mulcahy, M.J., Cohen, B., et al. (2019). Determining the pharmacokinetics of nicotinic drugs in the endoplasmic reticulum using biosensors. *J. Gen. Physiol.* **151**, 738–757.
- Sneddon, J.M. (1969). Sodium-dependent accumulation of 5-hydroxytryptamine by rat blood platelets. *Br. J. Pharmacol.* **37**, 680–688.
- Studier, F.W. (2005). Protein production by auto-induction in high density shaking cultures. *Protein Expr. Purif.* **41**, 207–234.
- Sun, F., Zeng, J., Jing, M., Zhou, J., Feng, J., Owen, S.F., Luo, Y., Li, F., Wang, H., Yamaguchi, T., et al. (2018). A Genetically Encoded Fluorescent Sensor Enables Rapid and Specific Detection of Dopamine in Flies, Fish, and Mice. *Cell* **174**, 481–496.
- Tatsumi, M., Groshan, K., Blakely, R.D., and Richelson, E. (1997). Pharmacological profile of antidepressants and related compounds at human monoamine transporters. *Eur. J. Pharmacol.* **340**, 249–258.
- Taylor, N.D., Garruss, A.S., Moretti, R., Chan, S., Arbing, M.A., Cascio, D., Rogers, J.K., Isaacs, F.J., Kosuri, S., Baker, D., et al. (2016). Engineering an allosteric transcription factor to respond to new ligands. *Nat. Methods* **13**, 177–183.
- R Development Core Team (2013). R: A language and environment for statistical computing (R Foundation for Statistical Computing).
- Tinberg, C.E., Khare, S.D., Dou, J., Doyle, L., Nelson, J.W., Schena, A., Janowski, W., Kalodimos, C.G., Johnsson, K., Stoddard, B.L., and Baker, D. (2013). Computational design of ligand-binding proteins with high affinity and selectivity. *Nature* **501**, 212–216.
- Wan, J., Peng, W., Li, X., Qian, T., Song, K., Zeng, J., Deng, F., Hao, S., Feng, J., Zhang, P., et al. (2020). A genetically encoded GRAB sensor for measuring serotonin dynamics in vivo. *bioRxiv*. <https://doi.org/10.1101/2020.02.24.962282>.
- Wang, H., Goehring, A., Wang, K.H., Penmatsa, A., Ressler, R., and Gouaux, E. (2013). Structural basis for action by diverse antidepressants on biogenic amine transporters. *Nature* **503**, 141–145.
- Wankerl, M., Miller, R., Kirschbaum, C., Hennig, J., Stalder, T., and Alexander, N. (2014). Effects of genetic and early environmental risk factors for depression on serotonin transporter expression and methylation profiles. *Transl. Psychiatry* **4**, e402.
- Wickham, H. (2016). *ggplot2: Elegant Graphics for Data Analysis* (Springer).
- Wickham, H., Averick, M., Bryan, J., Chang, W., McGowan, L., François, R., Grolemund, G., Hayes, A., Henry, L., Hester, J., et al. (2019). Welcome to the Tidyverse. *J. Open Source Softw.* **4**, 1686.
- Williams, G. (2011). *Data Mining with Rattle and R: The Art of Excavating Data for Knowledge Discovery* (Springer-Verlag).
- Wu, Z., Kan, S.B.J., Lewis, R.D., Wittmann, B.J., and Arnold, F.H. (2019). Machine learning-assisted directed protein evolution with combinatorial libraries. *Proc. Natl. Acad. Sci. USA* **116**, 8852–8858.
- Yang, K.K., Wu, Z., and Arnold, F.H. (2019a). Machine-learning-guided directed evolution for protein engineering. *Nat. Methods* **16**, 687–694.
- Yang, K.K., Chen, Y., Lee, A., and Yue, Y. (2019b). Batched Stochastic Bayesian Optimization via Combinatorial Constraints Design. *arXiv*, arXiv:1904.08102.
- Yokoyama, M., Suzuki, E., Sato, T., Maruta, S., Watanabe, S., and Miyaoka, H. (2005). Amygdalic levels of dopamine and serotonin rise upon exposure to conditioned fear stress without elevation of glutamate. *Neurosci. Lett.* **379**, 37–41.
- Zhang, Y.-W., Turk, B.E., and Rudnick, G. (2016). Control of serotonin transporter phosphorylation by conformational state. *Proc. Natl. Acad. Sci. USA* **113**, E2776–E2783.
- Zhou, X., Lu, J.Y.-F., Darling, R.D., Simpson, K.L., Zhu, X., Wang, F., Yu, L., Sun, X., Merzenich, M.M., and Lin, R.C.S. (2015). Behavioral training reverses global cortical network dysfunction induced by perinatal antidepressant exposure. *Proc. Natl. Acad. Sci. USA* **112**, 2233–2238.
- Zhuang, X., Masson, J., Gingrich, J.A., Rayport, S., and Hen, R. (2005). Targeted gene expression in dopamine and serotonin neurons of the mouse brain. *J. Neurosci. Methods* **143**, 27–32.